

Hillslope Angle, Grain Size, and Radial Transport: Coarse Sands Move Faster but Medium
Sands Dominate Flux

Table of Contents

Title Page	1
Table of Contents	2
Introduction	3
Methods	4
References	8
Appendix	9

Chapter I

Introduction

1.1 Introductory Hillslope Geomorphology & Motivation of Research

Hillslopes, defined as any natural angled surface constituting the flanks of valleys or eroding uplands, are perhaps the most ubiquitous landform on any natural body. Hillslopes, in their myriad forms, have always fascinated humankind; innumerable societies have granted mystical properties to these landforms, with some hillslopes and hill tops even being granted the status as the home of deities, or other places of spiritual significance (Homer, 700 B.C.E. a.; Homer, 700 B.C. b; *New King James*, Gen 22:2; Pommersheim, 1988). However, while it is likely that some scientists quantitatively investigated the evolution of hillslopes since antiquity, it was not until the development of critical thought in the geosciences that the ephemeral nature (with respect to geological time) of hillslopes was accepted.

In 1879 John Wessley Powell published his manuscript *Report on the Land of the Arid Regions of the United States* which amongst many other ideas suggested that rivers erode down to a “base level”, an elevation which behaves as datum which is the lowest possible erodible elevation on land. The implications of a base level or any fluvial system are two-fold: a river while eroding down to base level will create a channel, and second, by necessity, the river channel will be bounded by hillslopes. The science of hillslope evolution continued slowly and in 1899 W.M. Davis is credited with being the first individual to postulate that landscapes followed a “geographic” cycle of erosion: land, uplifted through some force, is slowly eroded to base level forming a flat peneplain with a minimally changing geometry until a new uplifting force acts upon it. However, modern hillslope geomorphology formally began with the work of G.K. Gilbert.

In 1909 G.K. Gilbert described the fundamental convex geometry of the hillslope. In his brief 1909 publication Gilbert describes the process of creep, the slow movement of soils down a hillslope via processes such as rain splash and frost heave. While he attributes this description of this process back to W.M. Davis (who published the original idea in 1892) it is G.K. Gilbert who formalized creep’s importance and role in sculpting a hillslope. Over the next 50 years hillslope geomorphology became increasingly quantified, with seminal publications by W.E.H Culling in 1960, 1963, and 1965 which formalized an analytical theory of erosion via diffusive processes and the role of soil creep as a depth distributive sediment transport process. Since the publications by Culling many more investigations have been undertaken, many of which will be covered in upcoming chapters. Despite nearly 150 years of published scientific study the fundamental processes that drive the evolution of hillslopes are still unknown.

Many of these unknowns regard a fundamental constituent of the hillslope itself: the soil mantle. Much has been studied on the formation and evolution of soils with respect to landform evolution (Darwin, 1881; Hans, 1941; Carson and Kirkby, 1972; Heimsath et al., 2005, Gray et al., 2019) yet many questions remain about the grain-scale dynamics of

landforms. All landforms are transient; a result of the granular particles composing the soil mantle undergoing transport via erosive processes. Therefore, to understand the evolution of any landform (or soil for that matter), an understanding of grain-scale transport is also necessary. Additionally, understanding the transport rates of sediment particles allows for better predictive modeling of geohazards such as mass wasting (Gonzalez de Vallejo and Ferrer, 2011), the sedimentation rates of lakes , rivers and reservoirs (Rose et al., 2010; Sklar et al., 2017), or the track of pollutants bonded to sediments (Jiang et al., 2020). Lastly, understanding the transport and dynamics of granular media is a broader goal for the physics community as dynamics of granular media shares a place with turbulence as one of the last great problems in classical mechanics (Gago and Boettcher, 2020). The following sections and chapters document the pursuit of further knowledge to understand the fundamental relationship between hillslope form and grain-scale transport process and rates.

1.2 Problem & Dissertation Objective

The spatial distribution of sediment grain sizes of a hillslope's soil mantle is expected to adhere to a hypothetical fit whereby the foot slope is enriched in relatively fine-grained particles and the crest of the hillslope is enriched in relatively coarse grain particles. This spatial distribution is particularly notable for landforms composed of glacially deposited material (Krumbein, 1940). This hypothetical spatial distribution can be found by measurement of grain size distribution of sediments at the crest, mid slope, and foot slope of hillslopes or by extrapolating the basic calculation of forces required to transport grains of any given size to a hillslope and the probability of force magnitude occurrence:

To transport a stationary particle, regardless of the transport inducing process, a shearing force must be applied to the particle sufficient to overcome the static friction (Pouliquen and Forterre, 2002; Louge, 2003). If this shearing force is not greater than the force of friction no motion will occur. The equation for the maximum force of static friction is

$$\vec{F}_f = \mu M \vec{G} \cos (\theta) \quad (1)$$

And thus, the following inequality must be satisfied to initiate particle motion:

$$\vec{F}_{shear} > \vec{F}_f \quad (2)$$

Where \vec{F}_f is the frictional force, \vec{F}_{shear} is an applied shearing force, μ is the coefficient of static friction, M is the mass of the particle, G is gravitational acceleration, and θ is the hillslope's angle.

We can rearrange Newton's second law of motion to find the acceleration of a particle given an applied force and an object's mass

$$\frac{\Sigma \vec{F}}{M} = \vec{A} \quad (3)$$

Where $\sum \vec{F}$ is the sum of all forces being applied to the particle and \vec{A} is the objects acceleration. By substituting in equation (1) into equation (3) and accounting for the applied shearing force we get:

$$\frac{\vec{F}_{shear} - \mu \vec{G} M \cos(\theta)}{M} = \vec{A} \quad (4)$$

By way of these equation 4, a smaller particle requires less applied force to overcome a static frictional force inducing particle motion.

We can continue this derivation by looking into the realm of statistical mechanics. Using the Boltzmann distribution:

$$p_i = \exp\left(-\frac{\varepsilon_i}{kT}\right) \quad (5)$$

Where p_i is the probability of energy in a system, ε_i is the energy of that state, k is the Boltzmann constant, and T is the thermodynamic temperature (Arfken et al. 2012). The Boltzmann distribution states that the energy of all system states is exponential in probability of occurrence. In other words, most of the time (and most applied forces) are small, and the probability of any given energy state or force decreases exponentially with greater magnitude. While the Boltzmann distribution was originally developed to describe physics of matter at atomic or molecular scales it has been discovered that it also applies, in principle, to granular media. For granular media the microscopic behavior of constituent atomic particles within the natural system creates emergent macroscopic behaviors with strong implications for sediment grain transport distances (Culling, 1963; Clarke et al. 1999; Furbish et al. 2021a, b, c, d).

Combining the results from equations 4 and 5, it would be expected that a hillslope's foot slope would be enriched in relatively fine grain materials since transport inducing force perturbations are typically small and so more frequent transport events occur due to a lower transport inducing event threshold.

In fact, has been found that sediment sinks (such as a delta or beach) are enriched in fine grain sediments compared to non-sink sedimentological counterparts (McLaren and Bowles, 1985). However, while this hypothetical spatial distribution of grains is expected to be ubiquitous on all mature hillslopes (as it is in larger sediment sinks) there is little published field data to verify this.

Evidence exists to suggest that many hillslopes do, in fact, have foot slopes enriched in relatively fine grain materials. However, much of the existing evidence suggests a more complicated relationship between regolith grain size distribution and transport rates as some hillslopes show a bimodal or multimodal distribution of grain sizes at both the crest and the foot slope (Wuenscher, 2018). Not only this, but transport rate experiments for particles $\leq 3\text{mm}$ in the field directly contradict the theoretical basis of transport built upon

in equations (1) and (2), even though overall transport rates of grains follow a power law distribution with respect to size (Madoff, 2015).

The purpose of this dissertation is three-fold. First, the surface transport rates of sand-sized sediment grains will be quantified at numerous field sites on a natural surface experimental hillslope. Since, by volume, most of a hillslope's soil mantle is composed of grains < 2 mm in diameter the grain sizes chosen for study over all experiments are within this size class. Specifically, tracer grains 2 mm and 0.75 mm along the longest axis are chosen for experimental analysis. Additional limited experiments investigating the surface transport rates of 30 mm pebbles are also undertaken to allow for a comprehensive analysis of surface grain transport rates. Second, the annual depth of the mobile sediment layer (hereafter "mobile layer") of the hillslope will be investigated along with the depth dependent transport rate of sediment grains. Lastly, the topographic evolution of the field site will be solved analytically (linear diffusion, and non-local transport) for comparison against a grain-based hillslope degradation simulation informed via field data, and broad field observations.

1.3 Background & Prior Research

Prior research into the transport rates and spatial grain size distribution of hillslopes is extensive. The following sections provide an overview of the most important concepts in the research of grain transport and granular flows, grain transport processes in natural systems, experimental investigations of grain transport, and modeling hillslope degradation based on observations of grain transport.

1.3.1 Physics of granular media

While the basic physics of initiating movement of any individual particle that is at rest are described in section 1.2, the physics relating to the interactions between grains in motion are more elusive, particularly when grains are exposed to high frequency vibrations, or when the grain pile reaches the angle of repose and begin to avalanche down the slope. In these conditions the body of grains may exhibit properties of a liquid or a gas rather than a solid (Van, 1945; Jaeger, 1992, Komatsu, 2001). In fact, there is no general theory for granular flows due in part to the high number of degrees of freedom that dictate particle-particle interactions for the entire granular body and the associated energy losses and non-local effects (Staron, 2008). Some authors have even suggested a new theory based upon statistical mechanics may be needed to describe the motion of granular flows (Jaeger, 1992). Due to this difficulty, thus far the most successful description of the physics of granular flows has come from individual scenarios which a granular flow may "experience".

One such model for granular flows includes the "bumpy incline model". In this model of granular flows the flow behavior is, in part, based on collisional rate-dependent inter-particle stresses along with existing inter-particle friction. In each flow there are four regions of different governing physics: first a base boundary layer where there is little energy transfer, a basal layer where grains slowly gain kinetic energy as the particles

transport down the bumpy slope, a flow core with constant kinetic energy, and a collisional surface where the inter-particle collisions rapidly reduce the available kinetic energy by transferring available energy to heat via friction (Pouliquen and Forterre, 2002; Louge, 2003). Additional evidence suggests that for granular flows over bumpy inclines the initial mode of transport at the collisional surface is bouncing, and as the velocity of the grain drops due to inter-particle collisions or frictional cooling the grains in the granular flow can become trapped in the rough surface with the probability of grain trapping decreasing linearly with the inclination of the plane (Henrique et al. 1998).

For much of the rest of this dissertation physics will be kept simple (such as equations 1-5) or when necessary be related to physics as described in Pouliquen and Forterre, 2002 or Louge, 2003. Non-local effects will also be addressed in the modeling section of this dissertation as non-local interactions between grain transport and hillslope form are well explored in the literature (See 1.3.5b).

1.3.2 Creep transport processes

Outside of large mass wasting events (rotational slides etc.) most of the transport processes causing regolith particles to transport downhill occur at slow rates. The collective term for these processes is *creep*, and each of these processes are discussed below (a list of global creep rates can be found in Oehm and Hallet, 2005).:

1.3.2a Tree-throw

Tree-throw is a sediment transport process in which vegetation (not necessarily trees) falls to the ground exposing their root systems sub-aerially. During the tree-throw process regolith is spread from the vegetable's root system in ballistic motion across all directions. While the net motion vector for particles is in all directions centered on the vegetable the greatest motion occurs in the downslope vector as this is the direction the vegetable is most likely to fall, and the total magnitude is directly proportional to hillslope gradient (Norman et al., 1995). The total sediment flux of tree throw can be considerable, with one study finding that a single weather-induced tree-throw event moving $1300\ m^3$ of sediment only via tree-throw.

1.3.2b Bioturbation

Much like tree-throw, bioturbation (the mixing and turnover of soil due to biological processes) is a significant process of sediment transport, while also being a significant source of soil mixing and transport mechanism for the entire mobile layer (Darwin, 1881; Gabet, 2000; Gabet, 2003). In the case of vegetation, the roots find their way into the soil to find the best sources of nutrients and water mixing and transporting soil as the roots dig. For animals, fossorial species such as gophers dig and burrow through the soil to consume plant roots and/or to make shelter. The effects of these processes are significant, with Hole, 1981 suggesting the dry weights of animal mounds may be between 5 and 70 tons per hectare for a given region dependent on animal species.

1.3.2c Frost Heave

Frost heave occurs when groundwater in the soil freezes, forming ice lenses that lift the soil upward. When these ice lenses melt, the soil subsides downslope (Taber, 1929). Although frost heave is a common process on many hillslopes, it rarely occurs in regions where the mean annual temperature remains below zero degrees Celsius. In contrast, areas characterized by frequent freeze-thaw cycles often experience frost heave as the dominant soil creep process, which can result in the formation of unique landforms.

1.3.2d Rain Splash

Rain splash occurs as precipitation impacts the soil surface sending regolith outward in ballistic motion away from the impact site due to momentum transfer (Furbish et al. 2007). On an inclined plane (such as a hillslope) the bulk of the grains eroded by rain splash are transported downslope (Carson and Kirkby, 1972). There is no clear calculation of global flux resultant from rain splash. However, it is agreed that particle trajectory increases with decreasing grain size, and hillslopes with the finest cohesionless grain size distributions have the greatest sediment fluxes from rain splash (Dunne et al. 2010).

1.3.3 History of quantifying creep, dry ravel rates, and hillslope degradation

Quantifying rates of creep in the field is challenging as the transport rates of sediments are low enough that they may not be visible to the observer, or occur with low frequency. The following sections outline the history of field-based creep experiments as well as laboratory experiments of regolith transport.

1.3.3a Creep rates on experimental natural hillslopes

The measurement of the transport of individual particles down hillslopes was first documented by Leopold et al. 1966 where the researchers tracked painted pebbles down the Gunshot Arroyo in New Mexico. Since this experiment, many other researchers have taken a similar approach. Kirkby and Kirkby, 1974 tracked grains > 1mm in diameter at 12 locations in Arizona and found that regolith transport rate was positively correlated with hillslope gradient and negatively correlated with grain size. A 16-year study by Abrahams et al. 1984 found that most transport in the Southwestern United States is directly related to hydraulic action, a finding also found by Kirkby and Kirkby, 1974 and Leopold et al 1966. Lastly, Perisco, 2005 found similar findings to Leopold, Kirkby, and Abrahams but also found that vegetation and bioturbation has a significant impact on pebble transport rates, with field sites containing significant vegetation having correspondingly lower transport rates compared to more smooth field sites.

Rates of creep from the surface to the bottom of the mobile layer have historically been measured via the insertion of an articulated tube perpendicular to the hillslope surface. After a specified time has elapsed (usually > 5 years), the soil to the immediate side of the inserted tube is excavated to reveal the transport rates of regolith with depth. The mobile layer has an infinite number of configurations and the transport rates with depth are

dependent on climate, soil parent material, flora, and fauna, and the mean transport rate decays approximately exponentially with depth (Carson and Kirkby, 1972; Komatsu, 2001). Unlike field-based individual grain experiments, there is significant data on hillslope creep with depth over long time scales, with sediment creep expected to be modeled effectively with continuum mechanics (Oehm & Hallet, 2005). In polar and alpine regions frost heave and thermal contraction are the primary cause of sediment transport down slope (MacKay, 1981; Smith, 1988; Jahn, 1991; Matsuoka, 1998; Putkonen, 2012) while in temperate and dry regions transport is dominated by hydraulic or biological processes (see references in prior paragraph).

While the prior cited research contained assumptions that soil behaves as a continuum process Clarke et al. 1999 found over a 23-year study that continuum models do not match their results, and determined that while long-term creep rates may appear to be continuous in nature, short-term disturbances are more likely to occur and “appear” to replicate continuum motion. Lastly, Heimsath et al. 2005 found that transport of soils on hillslopes is a function of the rate of soil production and hillslope gradient, with hillslopes containing a greater soil depth, higher soil production function, and greater hillslope angles having greater depth dependent transport of sediments than hillslopes with less soil and lower gradients.

More recent research has shown that sediments dry raveling (transporting down the hillslope not entrained in water) show different behaviors than that of sediments on hillslopes well below the angle of repose. Using field experiments and both 1-D and 2-D modeling Dibase et al. 2017 found that sediment flux increases with grain size and that for sediment grains undergoing long transport distances the transport distance is a function of hillslope angles and conditions upslope of the current hillslope angle along with the current hillslope angle and conditions (a phenomena termed non-local transport). Roth et al. 2020 also discovered similar phenomena on hillslopes recently unvegetated from wildfire, suggesting that continuum-based models do not capture the long distance particle transport that occurs at steep hillslope angles or vegetation-bare hillslopes.

While monitoring the transport of individual grains can provide clues as to the transport rates of individual particles over short time spans and mobile layer experiments using articulated tubes can provide mobile layer tracking over long time periods, to date (prior to this dissertation) there has been no good “in-between” to monitor short term mobile layer and surface transport rates. The best approximation of total sediment flux has historically been sediment traps. In these experiments, sediment traps are places at the bottom of a section of hillslope to collect transporting sediment. These sediment traps allow for the analysis of mobile grain sizes over short to medium time periods as well as the total sediment flux for that hillslope section (Wells and Wohlgemuth, 1987; Putkonen et al., 2007; Madoff, 2015).

1.3.3b Laboratory experiments

Laboratory experiments of sediment creep and surface transport have been conducted to reduce the variability that exists in natural systems. Roering, 2004 suggested sediment grains may only be entrained after a perturbation removed the grain from rest using acoustic experiments which created a concave-up mobile layer profile like profile found in field experiments. Furbish et al 2008 found that shearing force chains are required to entrain particles after the initial perturbative force that initiates motion. Both Roering, 2004 and Furbish et al. 2008 experimented across the full depth of the experiment hillslope in addition to the hillslope surface.

Gabet and Mendoza, 2012 investigated the transport of grains at the hillslope surface using laboratory experimental hillslopes and found that at low angled hillslopes transport distances of grains is approximately exponential while at steep hillslope gradients the distribution of grain transport distance is approximately uniform, with the transition from exponential to linear occurring near the angle of repose suggesting that the transition from local and non-local transport of grains occurs somewhere just below that angle of repose of the hillslope. Williams and Furbish, 2021 found that the transport distance of sediment grains depends significantly on grain shape, with angular grains transporting shorter distances than rounded grains and more transversely.

1.3.4 Weathering and Communion of sediment grains

Sediment grains, as with all else in the environment, undergo weathering processes that break down the sediment grains simply reducing the mass (simple weathering) or break the sediment grain into many small pieces (communition via weathering). Sediment grains may also undergo communition via mechanical processes such as grain-to-grain impacts (Ritter et al. 2011) Field evidence of weathering has suggested that granitic grains may weather at a rate of 0.01 – 0.3% mass while dolomite sediment grains may weather at a rate of 0.1 – 2% mass in tundra climates every year (Thorn et al 2006). While geochemical evidence in Antarctica suggests that even in extreme polar climates the crest of hillslope may lower at a rate of $\sim 2.1 \text{ m ma}^{-1}$ (Putkonen et al. 2008). In broader scope, field experiments of weathering of silicate minerals among many climates has found weathering rates of $10^{-14} \text{ m}^2\text{s}^{-1}$ to $10^{-17} \text{ m}^2\text{s}^{-1}$ over 10^4 to 10^7 years. In addition to simple mass weathering, Putkonen et al. 2014 has found that boulder communition in Antarctica occurs at a rate such that after an initial spalling event subsequent fragments spall at a rate 250 times slower than the initial spalling.

1.3.5 Soil mixing

Much of the knowledge of soil mixing with relation to sediment transport processes and rates comes from literature described in section 1.3.2b – bioturbation. Indirect studies of soil mixing has also been conducted using Optically stimulated luminescence dating (OSL), cosmogenic nuclide dating using $^{10}\text{Be}/^{26}\text{Al}$, and computer modeling. OSL and cosmogenic nuclides to determine soil mixing was first used in Heimsath et al. 2002 whose research found that soil grains repeatedly visited the surface while transporting through the

soil mantle towards the foot of the hillslope. Using similar methodologies Johnson et al. 2014 found that soil mixing decreases non-linearly with depth and that soil mixing is directly related to the change in flora root density with depth. Two companion papers, Furbish 2018a and Furbish 2018b found that, for most studies with available data up to 2018, OSL residence times for soil grains is distributed exponentially suggesting most soils are moderate to well mixed. A similar result was found in Gray et al. 2020 that showed soils mixed exponentially or linearly with depth and that soil mixing is likely an ubiquitous process across most climates.

1.3.6 Modeling Hillslope degradation

Modeling the effects of sediment transport processes on hillslope form may be completed via a variety of numerical methods. Most of the following methods are descriptive in nature. In other words, while they are based on real physical phenomena, they do not attempt to resolve changes in hillslope form on a transport-process level.

1.3.6a Linear and non-linear diffusion

In 1960 W.E.H Culling developed his analytical theory of erosion. In this theory, sediments transport from high density masses of materials to low density masses of materials in a similar fashion to the diffusion of heat in a metal bar, and that the flux of sediment is proportional to the hillslope gradient and can be modeled using continuum mechanics. In 1963 Culling extended his theory to include the seemingly random direction of sediment grains on a hillslope (soil creep). Finally, in 1965 Culling finished his theory of erosion by noting that the transport processes are indeed statistical in nature. The following derivation is a simplified version of the continuum derivation proposed by Culling, 1960:

The sediment flux parallel to topographic contour lines, q , is proportional to the hillslope gradient $\frac{\partial z}{\partial x}$:

$$q = -K \frac{\partial z}{\partial x} \quad (6)$$

Where K is the topographic diffusivity in $m^2 yr^{-1}$, a parameter than can be thought as a constant determining how “efficient” the hillslope is at shedding sediments. Topographic diffusivity values increases with latitude and has been estimated to be between zero and $1.5 \times 10^{-2} m^3 yr^{-1}$ depending on climate (Oehm and Hallet, 2005). Z is the hillslope elevation, and x is some horizontal distance along the hillslope. The negative of the right-hand term is taken with the assumption that sediments transport down the hillslope. Note that the gradient is provided in partial differential form; the partial differential is used since, in theory, the flux could be in any direction. If we take the first derivative of equation 6 with respect to elevation and time (t) we get:

$$\frac{\partial z}{\partial t} = \frac{\partial q}{\partial x} \quad (7)$$

The final form of the linear hillslope diffusion equation is therefore:

$$\frac{\partial z}{\partial t} = -K \frac{\partial^2 z}{\partial x^2} \quad (8)$$

This final form of the diffusion equation suggests that the sediment flux is not only linearly proportional to the hillslope gradient, but the second derivative suggests a smoothing of the hillslope profile over time. The linear diffusion equation is ubiquitously used to model landscape evolution (Fernandes and Dietrich, 1997) and allowed significant advances in understanding the ages of landforms and their degradation (Hallet and Putkonen, 1994; Martin and Church, 1997; Putkonen et al., 2008; Putkonen et al. 2008). While the linear diffusion model works well for hillslopes below the angle of repose, particularly for landforms composed of unconsolidated materials such as glacial moraines, linear diffusion models begin to perform poorly when the modeled landscape is near or above the angle of repose.

Roering et al. 1999 found that for hillslopes approaching or above the angle of repose landsliding became a more dominate processes when compared to simple sediment diffusion. Roering et al. 2001 and Roering et al 2007 continued to provide more evidence to support the predominance of landsliding near and above the angle of repose and a new equation for hillslope to account for non-linear dynamics of sediment transport processes was developed:

$$\bar{q}_s = \frac{-K \nabla z}{1 - \left(\frac{|\nabla z|}{S_c}\right)^2} \quad (9)$$

Where \bar{q}_s is the average sediment flux parallel to topographic contour lines, $-K$ is the same topographic diffusivity as in equations 6 and 8, ∇z is the hillslope gradient $\frac{\partial z}{\partial x}$, and S_c is the critical angle at which the sediment flux is expected to be infinite, and S_c is commonly taken to be the angle of repose for the hillslope in question. By using a Taylor expansion and substituting equation 9 into equation 7 we get the non-linear form of the diffusion equation:

$$\frac{\partial z}{\partial t} = -K \nabla z + K \left(\frac{|\nabla z|}{S_c}\right)^2 |\nabla z|^2 + \dots \quad (10)$$

While the linear diffusion equation was primarily used in the 20th century, many researchers have begun to use the non-linear diffusion equation to model hillslopes in more complex terrain, particularly for hillslopes whose are over steepened, since the non-linear form of sediment flux becomes increasing linear as the hillslope angle approaches zero (Martin, 2000; Foufoula-Georgiou et al. 2010; Ganti et al. 2012; Grieve et al. 2016; Doane, 2018).

1.3.6b Non-local sediment transport

While local and non-local models of sediment flux and hillslope diffusion have significant evidence to support their use for modeling the degradation of a hillslope profile over their lifetimes and at scales larger than individual grain disturbances, they do not consider the process that cause grain transport and the evolution of the landform at smaller scales (Furbish et al 2009). Indeed, the original formulation of hillslope degradation from Culling, 1963 and Culling 1965 was motivated from the statistically random processes occurring at the grain scale and the emergence of apparent diffusion at the landform scale. Evidence began to build starting from Clarke et al. 1999 who suggested that the small-scale short-term disturbances in soils led to the long-term apparent depth-depending creep of hillslopes and came to further fruition with Furbish et al. 2009 who developed a statistical description of sediment flux including bioturbation and related processes.

In 2010 three research groups independently developed a non-local formulation of sediment flux (Furbish and Haff, 2010; Foufoula-Georgiou et al. 2010; Tucker and Bradley, 2010). In the non-local formulation the sediment flux is viewed as a function not just of the local hillslope gradient (as is the view of the linear and non-linear forms of sediment flux) but rather as a weighted average of the gradients upslope of a point on the hillslope with weights decreasing with increasing distances of the measured point. Additionally, all three forms of non-local sediment flux approach the problem of sediment flux from a statistical mechanical perspective rather than a continuum mechanical perspective as had traditionally been the case with local and non-local forms of sediment flux and the resulting derivative research on depth dependent sediment creep. The following equation of the non-local form of sediment flux is taken from Foufoula-Georgiou et al. 2010 as this formulation is the most straightforward, albeit a continuum formulation for a statistically mechanical process chain:

$$q^* = -K^* \int_0^x g(l) \nabla z(x-l) dl \quad (11)$$

Where q^* is the non-local sediment flux, K^* is the non-local topographic diffusivity, $g(l)$ is a kernel performing a weighted average of upslope gradients to determine the strength of the non-local influence to point x , ∇z is the gradient at point x , and l is lag of particle transport. It should be noted that Cushman 1991 and 1997 show that equation 11 is a convolution of diffusion equations such as equation 8 above and that $g(l)$ has no characteristic length and scales as a power law with most of the influence being near point x and trailing off in the form of x^γ .

The modeling of hillslope surface grain transport takes significant inspiration from statistical mechanics since the seemingly random transport of grains has eluded the description of continuum mechanics (Furbish 2021a, b, c, d). As such, much of the research for surface grain transport in the geosciences (see section 1.3.1 for pure physical descriptions without concern for natural systems) has been in relation to non-local sediment transport theories. These non-local sediment transport modeling theories have been well developed in the papers cited in section 1.3.5b and compiled in the seminal series of papers on the subject by papers by Furbish et al. a, b, c, and d.

Following from the prior papers cited in section 1.3.5b the Furbish 2021 papers continue to develop a general theory for the rarefied motion of particles on hillslopes (rarefied defined by the intermittent entrainment and disentrainment of sediment grains). In this general theory of rarefied motion of sediment grains the transport distance of grains is found to be a generalized pareto distribution: that is, most sediment grains do not travel far, but a non-insignificant portion of grains travel significant distances. The generalized pareto distribution for the transport distance lengths was found to be:

$$f_x(x) = \frac{\frac{1}{B^A}}{(Ax+B)^{1+\frac{1}{A}}} \quad (12)$$

Where x is the particle travel distance, $f_x(x)$ is the generalized pareto probability distribution for particle transport distances, A is the pareto shape parameter and B is a pareto scale parameter. The derivation from Furbish et al. 2021a to get to the generalized pareto function for grain transport distances is lengthy, and thus I direct readers to that paper for the full derivation.

The results of Furbish 2021a also suggest that natural particles with a small diameter with respect to the overall surface roughness show a high probability of getting trapped within the pockets of the surface while larger particles may not get trapped. This finding is also present in Wiberg and Smith 1987; Kirchner et al. 1990; Henrique et al. 1998; and DiBase et al. 2017 where the authors of these papers found that grains became trapped in surface depressions.

There is significant evidence to suggest that sediment does indeed transport non-locally (Gabet and Mendoza, 2012; DiBase et al. 2017, Doane et al 2018; Roth et al. 2020). With the field evidence for non-local processes being covered in the sections in which these papers are introduced.

1.3.6c Creeping glass

In response to conflicting theories of sediment transport (local vs. nonlocal) some authors have attempted alternative formulations to hillslope evolution. One such alternative formulation was proposed by Houssais and Jerolmack, 2016 and improved upon in Ferdowsi et al. 2018 which suggests that the granular dynamics of soil mantled hillslopes can be modeled similar to a creeping glass. In these models the shearing of granular media is analogous to the shearing of molecules within a glassy solid. In contrast to the local and non-local models, the hillslope degradation models using the creeping glass analogy use discrete element method techniques to solve the evolution of a landform. Finally, experimental findings using laser and vibrational disturbances to a granular sand pile found that the sand pile degraded like a glass and distributed gains ala Culling-like diffusion, albeit from different granular mechanics than those proposed by Culling in 1963 (Deshpande et al. 2020).

1.3.6d Particle based

Particle-based hillslope degradational modeling has been used in place of non-linear sediment flux formulations when attempting to understand the mechanistic action behind non-linear hillslope diffusion. In these particle-based hillslope degradational models a uniform mobile layer of granular media is modeled along a uniform hillslope angle and solved using discrete element methods (BenDor and Goren, 2018). These particle-based models agree with non-linear sediment flux formulations from Roering, 1999 and related literature.

1.4 Field Sites

The field sites chosen for the analysis of fine grain sediment transport rates were moraines along the eastern front of the Sierra Nevada mountain range and within the Mono Basin of California (See figures 1 and 2). Very generally, the Sierra Nevada formed in the late Jurassic due to magmatic intrusions related to the subduction of the Farallon plate beneath the North American plate with subsequent uplift ~20 myr during the start of the Basin and Range extension event. A complete geological history of the Sierra Nevada is outside of the scope of this dissertation and is provided in Moores, 1999 and Hill, 2006. Mono Basin is suspected to be a tectonic – volcanic structural depression determined by gravity anomalies and volcanic activity within and along the southern and eastern edges of the basin (Williams et al. 1968).

The moraines deposited into the Mono Basin, the Mono Basin moraine and Tahoe moraine, were chosen for their ideal likely initial topographic conditions (Putkonen and Swanson, 2003) and apparent diffusive evolution. Additionally, the age of these moraines are well constrained as they are adjacent to one another with the Tahoe moraine cross cutting the Mono Basin moraine indicating that the Mono Basin moraine is older than the Tahoe moraine. Indeed, cosmogenic nuclide dating of boulders along the crest of these moraines indicate that the Mono Basin moraine was deposited ~100 kyr ago and the Tahoe moraine ~45 kyr ago (Phillips et al. 1990; Putkonen and Swanson, 2003; Gillespie and Clark, 2011).

Beyond these deposition events that led to the formation of the Mono basin and Tahoe moraines, 9 other glaciations have been identified. Table 1 below lists the glaciations in order from youngest to oldest glaciations, and is adapted from Gillespie and Clark, 2011:

Glaciation Name	Estimated ages (ka)	Reference
Little Ice Age (Matthes)	0.6 - 1	Stine 1994
Recess Peak	14.2 – 13.1	Clark 1997
Tioga	25 - 16	Phillips et al. 1996
Tenaya	31	Phillips et al. 1996
Tahoe II	50 - 42	Phillips et al. 1996
Mono Basin	80 – 60 (100)	Phillips et al. 1996 (revised using cosmogenic nuclides and numerical modeling in Putkonen, 2006)

Tahoe I	170 - 130	Phillips et al. 2009
Pre-Tahoe (Bloody Creek)	220 - 140	Phillips, 1990
Walker Creek	550	Clark 1968
Sherwin	820	Birkeland et al. 1980
Lower Rock Creek	920	Birkeland et al. 1980
McGee	2700 - 1500	Huber, 1981

Table 1. Ages of Sierra Nevada glaciations. Table adapted from Gillespie and Clark, 2011.

The National Weather Service monitoring site at Lee Vining provides the modern weather and climate data. Lee Vining sits at an elevation of 2,100 m and is 2.5 km north of the moraines. The mean annual temperature for Lee Vining is 9.55 °C and the town receives approximately 480 mm of precipitation each year (including snow water equivalent). The majority of the precipitation is in the form of snow, with an average annual snow depth of 0.58 m. For the snow free season (May-October), the mean annual precipitation reduces to 100 mm. The current elevation of the moraines at their most distal point from the Sierra Nevada is 2150 m and rises to a maximum elevation of 2600 m. Thus, it can be expected that the real mean annual temperature of the moraines is lower than Lee Vining, with the temperature reduced following the daily environmental lapse rate (Vasquez 2009). The real precipitation of the moraines is likely higher than Lee Vining as well to their higher elevation. The monthly summary of the air temperature, precipitation, and snow depth data from 1994-2024 is provided in the appendix.

The modern ecology of the moraines is typical of the semi-arid Great Basin ecotype. Below 2440 m on south aspect slopes, and below 2290 m on northern aspect slopes the surface of the moraines is dominated by sage bush species. Above the respective elevations for the slope aspects the vegetation is dominated by a mixed conifer zone transitioning into montane tree species at the maximum elevations adjacent to the Sierra Nevada mountain front (Erman 1996).

The Mono Basin and Tahoe moraines have been extensively studied for both basic research in Sierra Nevada paleoclimate and general hillslope and grain transport processes. Early paleoclimate research on the moraines began with Blackwelder, 1931 who mapped the moraines using simple field mapping techniques and progressed to cosmogenic nuclide dating techniques in Rood et al. 2011. The moraines in the area of the field sites are estimated to be between 2700 and 0.6 kyr old with the current interglacial period, excluding the little ice age, beginning around 11.5 kyr ago. Notably, the Mono Basin moraine cuts across the Pre-Tahoe and Tahoe I moraines and is itself cross cut by the Tahoe II moraine, and within the Tahoe II moraine exists lateral, terminal, and recessional moraines from the Tenaya and Tioga glaciations (Gillespie and Clark, 2011).



Figure 1. Redo this in ArcGIS



Figure 2. Redo this in arcGIS

Significant research has been conducted at the Mono Basin and Tahoe moraine field sites outside of pure local paleoclimatic work. The use of cosmogenic nuclides to date surface exposure ages was first suggested in Davis and Schaeffer, 1955 but it was not until Lal, 1991 developed an erosional model using paired nuclides that modern cosmogenic

nuclide dating took its current form. In 1994 Hallet and Putkonen refined the cosmogenic nuclide dating method for glacial moraines using the linear diffusion equation (equation 8) at the Tahoe moraine further refining of the technique for glacial deposits. Pukonen and Swanson, 2003 found that surface boulders of moraines may show distances up to 38% apart, and thus developed a method of boulder sampling, with the aid of the linear diffusion model, with data from the Tahoe moraine. Using the Mono Basin moraine as a field site, Putkonen and O'Neal, 2006 showed that diffusive degradation is likely occurring on all sloping unconsolidated landforms, and that this degradation interferes with cosmogenic nuclide dating techniques and Putkonen et al. 2008 found that due to diffusive sediment transport the original surface of glacial moraines is removed shortly after deposition increasing surface boulder frequency. Using paleoclimatic data as a guide and a space-for-time substitution, Madoff, 2016 found that a time-varying diffusivity constant provides a better result of moraine profile degradation than a simple non-varying diffusivity constant for moraines in the Sierra Nevada, including the Mono Basin moraine.

Additional significant research on sediment transport has occurred at the Mono Basin and Tahoe moraines. Work by Doane et al 2018 found that non-local and non-linear diffusion modeling better models the evolution of the moraines at the crest and foot of the moraines when compared to the linear diffusion model. The master's thesis, Weunscher, 2018, identified peculiar transport phenomena at the moraines; with 3 mm diameter aluminum tracer grains transporting at a greater rate than 0.7 mm aluminum tracer grains suggesting that grain transport velocities for sand-sized grains does not increase with decreasing size nullifying the hypothesis from equations 1-5. However, a grain-based degradational model shows that grains of this size are indeed the grains with the greatest flux across all grain sizes on the moraines, a finding backed by the enrichment of this grain size at the foot of the hillslope.

Work by Putkonen et al. 2008 and Weunscher, 2018 suggests that spatial grain size distributions of the hillslope have changed significantly over the lifetime of the moraines. The modern spatial distribution of the sediment grain sizes for the Tahoe moraine is found in figure 3 and the spatial distribution of the sediment grain sizes for the Mono Basin moraine is found in figure 4. A typical environment near the moraine crests of the moraines is in figure 5 and the typical moraine surface of the moraines at the midslope is in figure 6. The composition of the sediment grains is derivative of the material of the Sierra Nevada immediately upslope from the moraines (where the glaciers originated from) and is composed mostly of granitic and metavolcanic clasts. Additional clasts from recent volcanic eruptions within Mono Basin have also added surface clasts of obsidian and pumice.

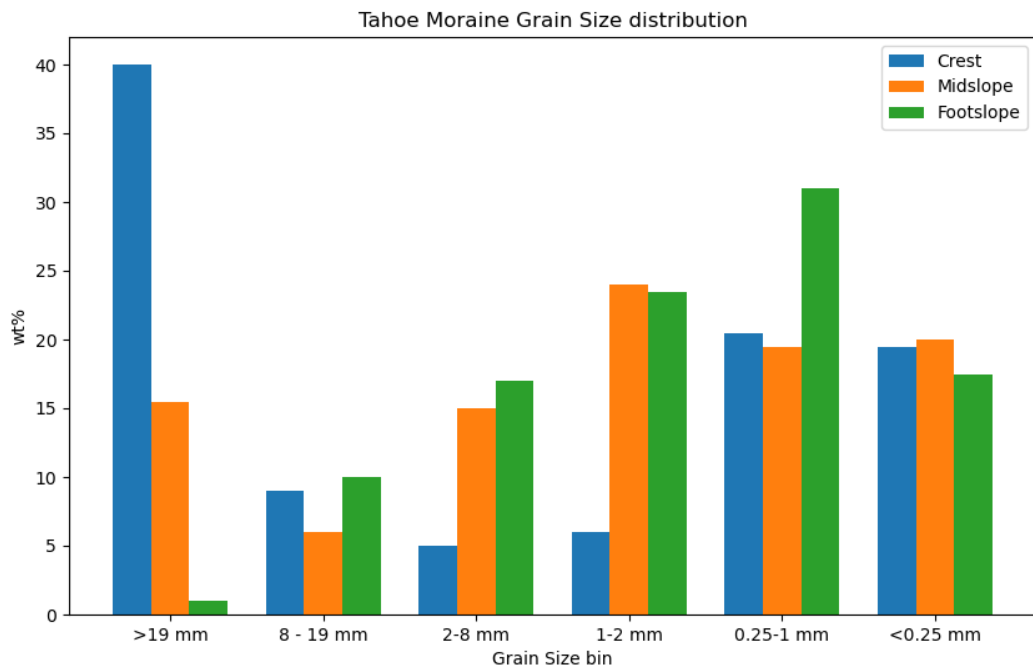


Figure 3. The grain size distribution of the Tahoe moraine for the crest, midslope, and footslope. The data is an averaged composite of Weunscher, 2018 and this study.

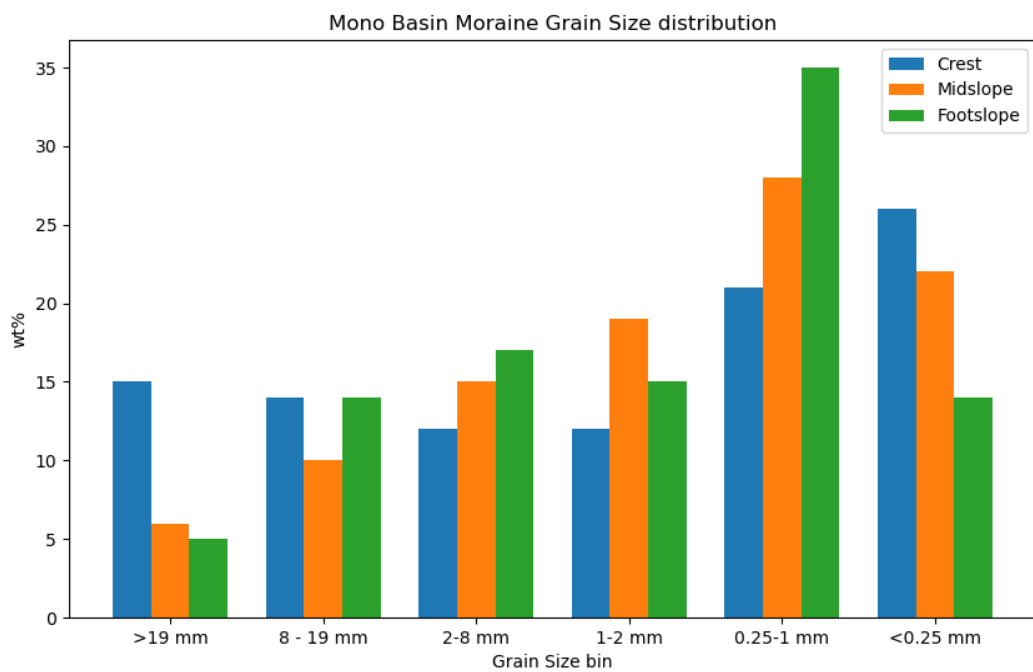


Figure 4. The grain size distribution for the crest, midslope, and footslope of the Mono Basin moraine.



Figure 5. The typical environment 10 m below the crest of the Mono Basin moraine. The larger boulder in the foreground is approximately 1.5 m in diameter.



Figure 6. Typical surface of the Mono Basin and Tahoe moraines midslope. Note the bioturbation tunnels on the right of the image.

Chapter 2

Methods

2.1 Field site selection

Field sites were determined based upon available hillslope angles, available space between clearings of sage, and representative hillslope surfaces. Many hillslope angles were available below 10 degrees and above 15 degrees. Only one site was measured between 10 and 15 degrees despite the average overall angle of both moraines being within this range. All field sites had at least 2 m of distance between the highest elevation sage and lowest elevation sage and a width between sages of at least 3 m. Field sites at angles greater than 15 degrees were located in sage clearings approaching the minimum available size while significantly larger sage clearings had lower hillslope angles. Whenever possible all field sites were placed directly within the fall line of one another such that an estimation of the sediment flux could be reasonably estimated along that line on the hillslope for that year.

Once a field site was found, pictures are taken of the field site in both a macro shot to display the general surroundings as well as micro shots showing the typical appearance of the regolith. Notes are taken on the hillslope angle, field site coordinates, hillslope aspect, experiment type, vegetation present, condition of the field site (pockmarked vs smooth), presence of animals, and other notable features. After these notes are taken the field experiments are set up. Pictures of the variable field site surfaces are found in figures 5, 6, 7, 8, 9, 11, and 12.

2.2 Surface transport rate sites

Surface grain transport was quantified by via measurement of the displacement of glass tracers at the field sites over one-year intervals. Two types of surface tracer field sites were developed.

2.2.1 30 mm particle field sites

The first type of surface transport field site measured the transport rates of 30 mm rock fragments. These field sites were first marked by two 0.5 m sections of rebar spaced 2 m apart with the expected sediment flux perpendicular to the paired rebar placement. Rock fragments were spaced 0.1 meters apart with a total of 20 rock fragments placed at each experiment site. Each rock fragment was numbered, and the position of each rock fragment was noted. After one year the horizontal and lateral displacement of each rock fragment was measured to calculate the absolute displacement from the fragment's original position. The experiment was then reset for another measurement the following year.



Figure 7. Example of pebble line one year after setting the experiment. Pebbles are approximately 30 mm in diameter along the widest axis. Hillslope angle was approximately 12 degrees.

2.2.2 2 – 0.75 mm particle field sites

The second type of field site measured the transport rates of 2 and 0.75 (range 0.5 – 1mm) glass tracer particles (density $\sim 2.5 \frac{g}{cm^3}$). Glass tracer particles were chosen as a proxy for natural field materials since marking natural field materials such as done with the 30 mm particles does not scale well with decreasing particle size (the low mass of small particles precludes painting and other types of marking). Field sites were marked in the same way as the 30 mm tracer sites, except the rebar was placed 0.5 m apart for easier post experiment tracking. Both bead sizes were placed together between the rebar in a circle with a diameter of ~5 cm centered on the middle point between the rebar. The exact location of placement of the field site was central and in the upper 70% of the sage clearing on a representative hillslope surface. For all field sites ~500 and ~3000 beads of 2 mm and 0.75 mm beads were placed, respectively. This distribution does not match the grain size distribution of the hillslope since matching the grain size distribution would cause difficult tracking of larger grain sizes and reduce overall tracer grain recovery rates. Due to this, the total flux for the field sites is later corrected using the grain size distribution.



Figure 8. 0.75 (blue tracers) and 2 mm (black tracers) set up for the surface transport experiment.

Samples were then collected one year later using 9.5 cm wide and 20 cm long brick laying molds along the hillslope fall line starting at the initial tracer placement point (0 cm tracer displacement) down to 76 cm below the initial placement point and an additional measurement 100 cm below the initial placement point. Upslope samples were taken at the same intervals up to 28.5 cm above the initial placement point to measure any upslope particle transport. All samples were approximately 1 kg in total mass and were taken from the surface down to ~6 cm in depth and over the entire width of the brick laying mold (Fig. 10). All samples were taken to the lab to count glass particles for determination of grain transport rates.



Figure 9. Example of moraine surface after surface tracer experiment. Note the red arrows pointing to the surface tracers. The blue tracers in the center and upper right are a minimum of 0.5 mm and a maximum of 1 mm in the longest axis while the black tracer (bottom right) is 2 mm in the longest axis. The minimum axis (shown in the photograph) is about 1 mm.

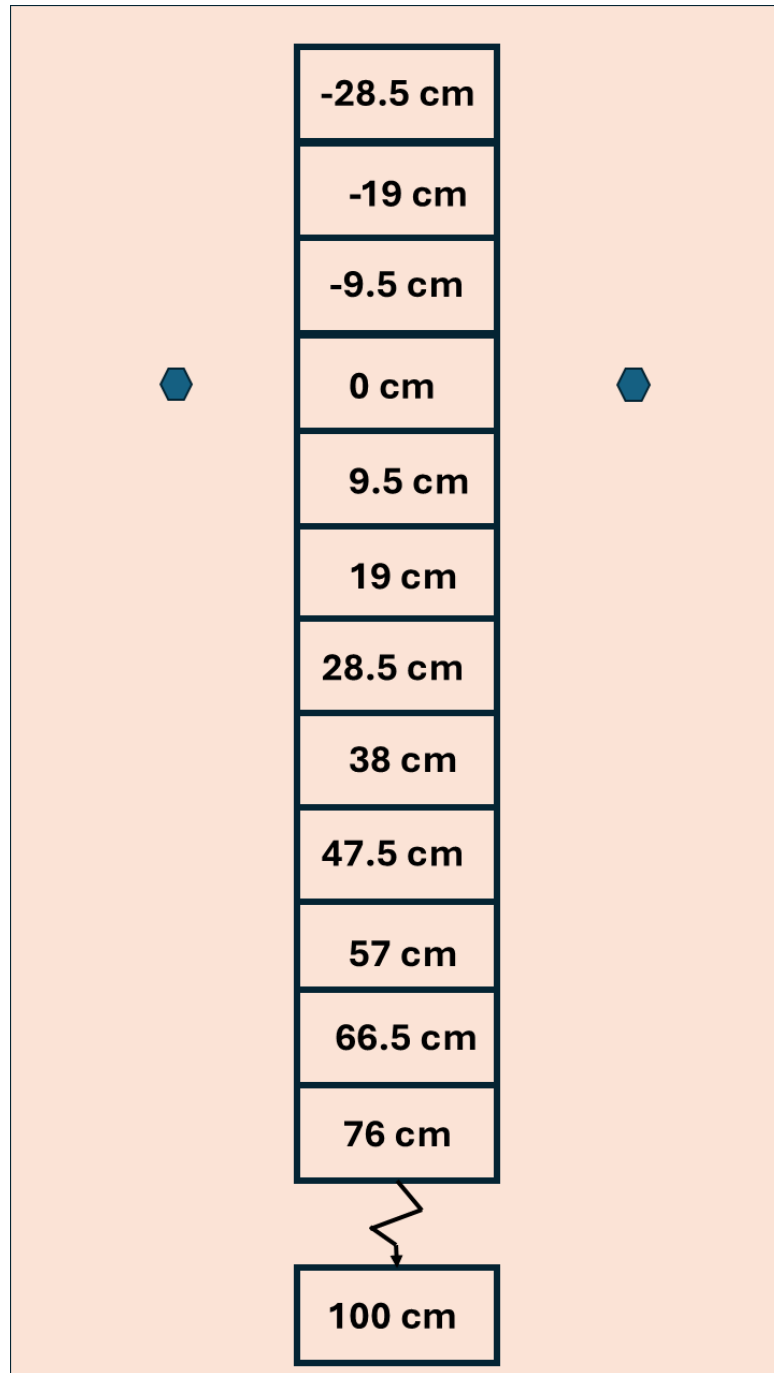


Figure 10. Surface tracer sampling schematic. The tracers were placed centrally between two rebar (blue hexagons). The sampling instrument was a 9.5 cm long, 25.4 cm wide brick laying mold. After arriving to the field sites one year post tracer placement the first sample was taken between the rebar so that the original tracer placement pile would have been inside of the brick laying mold. Any tracers collected from this first sample would have their transport considered to be zero cm. The brick laying mold would stay in-situ while a second brick laying mold is placed upslope the first brick laying mold and a third brick laying mold is placed downslope of the first. Tracers collected in brick molds two and three have transport distances of -9.5 cm (upslope of the original placement point) and 9.5 cm (9.5 cm below the original placement point) respectively. The process continues so that samples are taken up to -28.5 cm and down to 100 cm with a break between 76 and 100 cm.

2.3 2 – 0.75 mm particle displacement calculation

To determine 2 and 0.75 mm particle transport rates field samples were first sieved by grain size and then sub samples were taken of each sieved sample in the lab. Sub samples were taken since the total number of tracer grains within the sample were often too large to effectively count (>1000 for 0.75 mm tracers) for the number of samples taken). Each sub sample was 25% of the total sieved sample mass, and sub samples were randomized by thoroughly mixing the samples by hand prior to sample retrieval. Sub samples were retrieved from the mixed sieved sample by simply scooping small masses of material until 25% of the total sample mass was taken. All masses were determined using a 1000g scientific balance with 0.001g precision.

To determine the number of glass tracers in each sub sample the sub samples were spread onto a aluminum tray and visually inspected. When a glass tracer was found the glass tracer was removed from the sub sample with a tweezers. This process continued until no more glass tracers were found in the sub samples. This process was performed for both the 2 mm and 0.75 mm glass tracer particles. To bring the particles counted in the sub sample to parity with the full sample the sub sample count was multiplied by four. The final adjusted particle sample count was then tracked in a spreadsheet for further use later for modeling and flux calculation purposes.

2.4 Surface tracer creation and selection

All surface tracers < 30 mm in diameter were developed from glass beads of the brand **bead brand** which has a density of 2.5 g/cm^3 (field regolith density is $\sim 2.65 \text{ g/cm}^3$). 2 mm surface tracers were created by simply sieving the commercially available tracers (11/0 size) with a 2.36 mm sieve and 1.981 mm sieve to ensure a uniform 2 mm diameter. 0.75 Glass tracers were created by smashing the 11/0 size beads with a 1.5 kg rock hammer and sieving the smashed glass shards with a 1 mm sieve and 0.589 mm sieve and to ensure a uniform 0.5 – 1 mm diameter (mean diameter 0.75 mm).

Surface tracers > 30 mm in size were rock fragments collected from the field site. These larger tracers were painted white for visibility and subsequently numbered for field tracking.

2.4.1 Glass surface tracer geometry and mass

It should be noted that glass tracer geometry is not the same between grain sizes, with the 2 mm grains having a torus geometry while the glass shards have a prismatic geometry. This geometry was not intentional. Rather this geometry was a result of a limitation of available tracer materials of a suitable size. Tumbling methods using a hobby rock tumbler was attempted to smooth out prismatic glass tracer particles unsuccessfully. It should be noted that while the geometry differs between the 2 mm and 0.75 mm particle sizes the relative surface area of the 2 mm particles is greater than the 0.75 mm particles. Additionally, the geometry of the 2 mm particles is such that the central hole within the

tracer is prone to regolith capture which creates a variable particle to particle mass between each 2 mm particle in the experiment further increasing the spread of uncertainty in grain transport rates. (Insert picture of grain geometries)

2.5 Mobile layer experiment placement

Hillslope sediment mobile layer experiments were set up near surface tracer field sites to get an estimation of regolith grain transport with depth in addition to the surface. At these field sites only 2 mm grains were placed due to the difficulty of quantifying 0.75 mm grains in experimental practice runs in the laboratory. Each field site is marked by two rebar with a space of 10 cm between the rebar. A 1 cm diameter hollow pipe, containing an inset solid pipe, is inserted perpendicular to the hillslope surface to a depth of 7 cm in the middle point between the rebar pair. After pipe insertion, the inset solid pipe is removed leaving behind the hollow pipe (fig 11). Next, 2 mm glass tracers of different colors are inserted into the placed hollow pipe such that each color spans a depth of 1 cm. To calculate how many beads to insert into the pipe so that a 1 cm depth of each bead color is achieved, a graduated cylinder was used to measure bead volumes. Since the graduated cylinder had a large diameter than the hollow insertion tube, algebra was used to calculate how far to fill the graduated cylinder:

$$\pi r_1^2 h_1 = \pi r_2^2 h_2 \quad (13)$$

Where π is the Greek constant, pi, r is the radius of the cylinders, and h is the height of the cylinders. Equation 13 is solved algebraically for the height so that a proper height to fill the larger graduated cylinder is used. After the graduated cylinder is filled to the calculated mark the beads are poured into the hollow tube. To ensure that the glass tracers are properly placed, after the insertion of each bead color the beads are gently tamped down with the solid pipe to ensure a flat surface. After all beads are inserted into the hillslope the hollow pipe is carefully removed from the hillslope leaving the inserted beads in-situ (fig 12). The beads are confirmed to be placed correctly when after the hollow tube is removed from the hillslope surface the final color of the glass tracers are flush with the hillslope surface. The glass tracers are then left in-situ for one year before field analysis is completed at the field site. The ideal mobile layer set up, in cross section, is in fig 13.



Figure 11. Setting up the mobile layer experiment. Further explain the procedure in this caption



Figure 12. End stage of mobile layer experiment set up. 2 mm tracers are flush with the hillslope surface with different colored tracers of equal diameter set at 1 cm intervals below the surface.

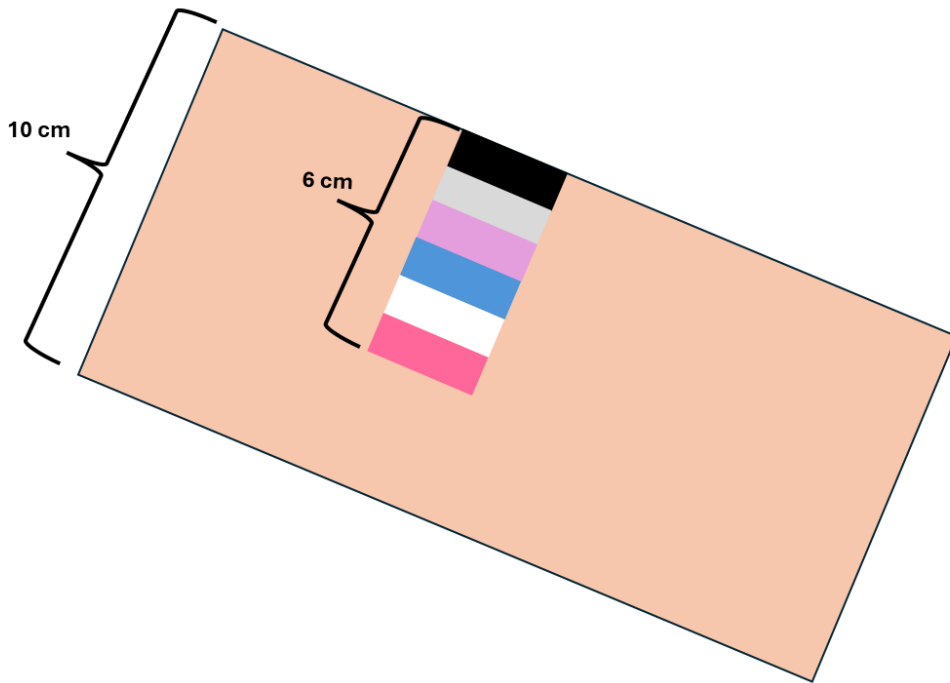


Figure 13. The ideal set up of the mobile layer in cross section. The six different colored beads are placed perpendicular to the hillslope surface and each tracer zone is exactly 1 cm in depth.

2.6 Mobile layer experiment analysis

After one year has elapsed the field sites are returned to for experiment analysis. First, notes are taken at the field site about the visual maximum displacement distance of glass tracers on the surface to guide the data recovery process. Recovery of subsurface data then begins by using a paintbrush (**Name of paintbrush here**) to slowly remove surface regolith exposing sediments at depth. This process begins at a minimum of one meter below the initial placement point along the hillslope fall line, and the surface is brushed down to a depth of 10 cm to expose the entire expected mobile layer, and the lateral swath is 25 cm to cover the entire expected fall line. Depth as determined by placing a 1 m flat object across the hillslope fall line at the point of measurement to approximate the average hillslope surface. Depth was then taken from the bottom of that proxy surface.

When a glass tracer is found the distance from the initial placement point is noted as well as the tracers depth. In many circumstances (particularly near the initial placement point) there are too many beads to measure individually. Thus, a general measurement is taken for each of the tracer colors in these cases. The result of these measurements (for each color) is the maximum transport distance, minimum transport distance, maximum depth, minimum depth, and a semi-quantitative measure of tracer mixing.



Figure 14. Mobile layer experiment excavation: The surface of the moraine is gently brushed away exposing the buried tracer grains. The minimum and maximum transport distances for each color tracer is noted as well as the minimum and maximum depth. Additional notes were taken on the condition of the field site and any other noteworthy observations. Here you can see the transport of beads down the hillslope including the excavation path. Note the black beads that are compacted into the regolith and not exposed at the surface indicating surface burial.

2.7 Random Grain Transport Simulation

While the goal of the surface tracer experiments is to retrieve all tracers placed in the field to accurately calculate sediment grain displacement distances, it has been shown to be infeasible to even collect larger tracer grains (3 mm diameter) with a 100% recovery rate (Wuenscher, 2018). Therefore, a computer model of random grain transport, guided by the field tracer experiments, will be developed to correct for the missing tracer data. The computer model was written in python 3.12.

The model contains a discretized grid space containing 200 pixels in the y direction and 100 pixels in the x direction with each pixel having a square geometry with 1 cm side lengths. The grid is given a surface roughness value based on the measured roughness of the hillslope field sites. The field surface roughness was measured by placing a flat meter stick onto the hillslope surface and taking measurements from the bottom of the meter stick to the hillslope surface every 5 cm. The average depth was then calculated along with the standard deviation from the average measured depth. The field surface roughness is applied to the model grid space on a per pixel basis by normally distributing the surface roughness across all pixels using the standard deviation as the model surface roughness. Lastly, the grid is provided an angle to create an inclined plane, and a virtual sample boundary is created to simulate the spaces sampled in the field.

The model is initialized with 1000 virtual tracer grains, with a percentage of grains set to not move at all through all the simulation time iterations. For each time iteration a grain is given a probability of movement chosen from a probability in the exponential distribution (as a result from equation 4) and a probability for either a directly downslope transport process or radial transport process. The transport logic for the directly downslope transport is simple, and only allows the tracer grain to move to the next adjacent grid pixel with the lowest gradient which will always be downhill due to the nature of the inclined plane. The radial transport process allow transport to any adjacent pixel in the grid with a small bias towards the pixel downslope with the greatest gradient.

The following model parameters are adjusted in the simulation to match the observations of the field experiments: the number of grains that do not move in each iteration, the probability of transport process (radial or downslope), and transport probability distribution shape. The model was run at 5 degree angles starting at 5 degrees and ending at 25 degrees. The model is stopped after the percentage of grains left within the sample boundary matches the number of grains recovered in the field. To determine if the model output for any given model parameters fit the field observations the model results for tracer distances are output in histogram format and compared to the histogram of transport distances from the field sites.

2.8 Numerical simulation of hillslope degradation and grain size distribution evolution

Excel was used for spreadsheet data entry, data tracking, and simple graph development. All numerical simulations were completed in Matlab 2023b and the full code for the models can be found in the appendix along with the interpolated moraine elevation data.

2.8.1 Numerical simulation of hillslope degradation using the linear diffusion equation

Hillslope degradation can be modeled as a function of the sediment flux along the hillslope. Therefore long-term degradation of hillslopes below the constituent material's angle of repose may be modeled simply using the linear hillslope diffusion equation (equation 8). The initial condition of the hillslope after deposition is assumed to have a hillslope angle of 31 degrees and a triangular cross section, which is the angle of repose for sand-sized particles (Van, 1945) and a common cross section for freshly deposited glacial moraines (Hallet and Putkonen, 1994). The simulation time set to the estimated age of the Mono Basin and Tahoe moraines was 100 kyr and 45 kyr respectively based on studies from Hallet and Putkonen, 1994; Putkonen and Swanson, 2003; and Weunscher, 2018. The value of K was determined via experimentation such that as the simulation runs from initial conditions a match is found to the current hillslope conditions. The model was solved using the finite difference method.

2.8.2 Numerical Simulation of hillslope degradation using Non-Local degradation

Since the transport of sediment has been shown to have a non-local component the change in the Tahoe and Mono Basin moraine form was also modeled using the non-local form of sediment flux, equation 11. The initial conditions for the non-local model are identical to that of the local diffusion model.

To reflect the influence of upslope conditions the decay scale was set to 50 m to reflect the long length of the moraine hillslopes (>50m) and the possibility of long grain transport distances when hillslopes are near the angle of repose (Roering et al. 1999; Furbish et al 2010). The real effect of this decay scale is such that no cell within the simulation will receive influence of degradation from any other cell outside of 50 m along the x-axis, and the influence of cells within the grid decays as a power law with distance from the current cell being modeled (Cushman 1991, 1997). The elevation at the grid cell being modeled is then changed based on the first derivative of the calculated non-local sediment flux.

2.8.3 Grain-based hillslope degradation simulation (GBHDS)

A grain-based hillslope degradation simulation driven by the linear diffusion equation and informed with field experiment data was written to provide a more detailed alternative to hillslope modeling compared to the diffusion of non-local models alone. Details on the architecture of the model can be found in section 2.7.4. The model is significantly adapted from the model first presented by Wuenscher, 2018.

2.7.4 GBHDS architecture

The GBHDS begins with an initialization of an idealized hillslope at the angle of repose (30 degrees for both the Tahoe and Mono Basin moraines). The idealized hillslope profile is discretized, and an initial grain size distribution is provided to the model. The initial grain size distribution for the moraines are approximated from the crest of the Tahoe Moraine, as the sediments at the crest are hypothetically the least weathered. Thus, these grain size distribution at the Tahoe moraine crest should be closest to the original grain size distribution post deposition. Once the grain size distribution is initialized the hillslope diffusion process begins.

To simulate hillslope degradation, the GBHDS defines transport rates of five grain sizes using diffusion coefficients (grain sizes: < 1 mm, 1 – 2 mm, 2 – 8 mm, 8 – 19 mm, > 19 mm) and a weathering constant for each grain size that combines the effects of the chemical and physical weathering leading to comminution. Each cell in the model has defined distance coordinate, elevation coordinate, and grain size distribution. The elevation of each cell in the model changes up or down in each time step based upon the linear diffusion equation whose total diffusion constant is the sum of the individual grain-size constants.

At each time step the weathering constant is applied to each grain size such that a small percentage of each grain size degrades to one size bin smaller, with the < 1 mm size bin being the smallest possible grain size. Additionally, in each time step sediment grains for each grain size diffuse from one cell to the next based upon the given diffusion coefficient of each grain size and hillslope gradient. As the model progresses through time the grain size distribution changes via diffusion of grains and grain weathering.

To find the best-fit GBHDS model for the Tahoe and Mono Basin moraines Latin-Hypercube Sampling (LHS) was utilized to find the initial best-fit diffusion and weathering coefficients. Latin Hypercube sampling works by iterating over randomly sampled input variables constrained by bounds and returning the values of model outputs using the randomly chosen samples. The diffusion coefficient bounds for the Latin-Hypercube sampling were defined by the approximate transport rates found by the surface grain field experiments and the weathering coefficient bounds via estimation from numerous model runs prior to LHS. To determine the best fit, the Root Mean Square Error (RMSE) was calculated for the final model profile against the measured hillslope profiles (measured at the field sites) and the grain size distributions at the moraine crests, midslope, and foot.

Once LHS has found the variables that produce the lowest error the input variables are manually adjusted to find an even more optimal solution to the model. After the diffusion and weathering coefficients have reached their maximally optimal solutions the initial grain-size distribution is changed within +/- 10% of the Tahoe moraine's crest grain size distribution.

2.7.5 Comparison of linear diffusion, non-local, and GBHDS models

To find the model that best fits the true profile of the Tahoe and Mono Basin moraines the RMSE is calculated between a transect of measured moraine profiles (measured directly along the field site locations) and the linear, non-local and GBHDS models. To make the

measured moraine profiles match the model output moraine profiles the measured moraine profiles were interpolated to match the grid system used in the computer models. To match the interpolated profile to the model outputs the location of the measured field sites were aligned with the model monitoring cells at the footslope. The model with the lowest overall error will be considered the best model for simulating the change in hillslope form over time.

References

- Abrahams, A. D., Parsons, A. J., Cooke, R. U., & Reeves, R. W. (1984). Stone movement on hillslopes in the Mojave Desert, California: A 16-year record. *Earth Surface Processes and Landforms*, 9(4), 365–370. <https://doi.org/10.1002/esp.3290090409>
- Arfken, G. B., Harris, F. E., & Weber, H.-J. (2012). *Mathematical methods for physicists* George B. Arfken ; Hans-Jurgen Weber ; Frank E. Harris. Elsevier.
- Birkeland, P.W., Burke, R.M., Walker, A.L., 1980. Soils and sub-surface weathering features of Sherwin and pre-Sherwin glacial deposits, eastern Sierra Nevada, California. Bull. Geol. Soc. Am. 91, 238–244.
- BenDror, E., & Goren, L. (2018). Controls over sediment flux along soil-mantled hillslopes: Insights from granular dynamics simulations. *Journal of Geophysical Research: Earth Surface*, 123(5), 924–944. <https://doi.org/10.1002/2017jf004351>
- Blackwelder, E., 1931, Pleistocene glaciation in the Sierra Nevada and Basin and Ranges: Bulletin of the Geological Society of America, v. 42, no. 4, p. 865-922.
- Carson, M. A., & Kirky, M. J. (1972). *Hillslope form and process*. University Press.
- Clark, M.M., 1968. Pleistocene glaciation of the upper West Walker drain age, Sierra Nevada, California. Geological Society of America Special Paper, 115, 317.
- Clark, D.H., Gillespie, A.R., 1997. Timing and significance of late-glacial and Holocene glaciation in the Sierra Nevada, California. Quatern. Int. 38 (39), 21–38.
- Clarke, M. F., Williams, M. A., & Stokes, T. (1999). Soil creep: Problems raised by a 23 year study in Australia. *Earth Surface Processes and Landforms*, 24(2), 151–175. [https://doi.org/10.1002/\(sici\)1096-9837\(199902\)24:2<151::aid-esp964>3.0.co;2-g](https://doi.org/10.1002/(sici)1096-9837(199902)24:2<151::aid-esp964>3.0.co;2-g)

- Culling, W. E. (1960). Analytical theory of erosion. *The Journal of Geology*, 68(3), 336–344. <https://doi.org/10.1086/626663>
- Culling, W. E. (1963). Soil creep and the development of Hillside Slopes. *The Journal of Geology*, 71(2), 127–161. <https://doi.org/10.1086/626891>
- Culling, W. E. (1965). Theory of erosion on soil-covered slopes. *The Journal of Geology*, 73(2), 230–254. <https://doi.org/10.1086/627060>
- Cushman, J. H. (1991). On diffusion in fractal porous media. *Water Resources Research*, 27(4), 643–644. <https://doi.org/10.1029/91wr00162>
- Cushman, J. H. (1997). The Physics of Fluids in Hierarchical Porous Media: Angstroms to Miles, 467 pp., Kluwer Acad., Norwell, Mass.
- Cushman, J. H., & Ginn, T. R. (2000). Fractional advection-dispersion equation: A classical mass balance with convolution-fickian flux. *Water Resources Research*, 36(12), 3763–3766. <https://doi.org/10.1029/2000wr900261>
- Darwin, C., 1881, The Formation of Vegetable Mould, through the Actions of Worms, with Observations on Their Habits, John Murray, London, UK.
- Davis, W. M. (1892). The convex profile of bad-land divides. *Science*, 245–245. <https://doi.org/10.1126/science.ns-20.508.245>
- Davis, W. M. (1899). *The geographical cycle*.
- Davis, R., Schaeffer, O.A., 1955. Chlorine-36 in nature. Annals of the New York Academy of Sciences 62, 107-121.
- Deshpande, N., Furbish, D., Arratia, P., & Jerolmack, D. (2020). *The Perpetual Fragility of Creeping Hillslopes*. <https://doi.org/10.31223/osf.io/qc9jh>
- DiBiase, R. A., Lamb, M. P., Ganti, V., & Booth, A. M. (2017). Slope, grain size, and roughness controls on dry sediment transport and storage on steep hillslopes. *Journal of Geophysical Research: Earth Surface*, 122(4), 941–960. <https://doi.org/10.1002/2016jf003970>
- Doane, T. H., Furbish, D. J., Roering, J. J., Schumer, R., & Morgan, D. J. (2018). Nonlocal sediment transport on steep lateral moraines, eastern Sierra Nevada, California, USA. *Journal of Geophysical Research: Earth Surface*, 123(1), 187–208. <https://doi.org/10.1002/2017jf004325>
- Dunne, T., Malmon, D. V., & Mudd, S. M. (2010). A rain splash transport equation assimilating field and laboratory measurements. *Journal of Geophysical Research: Earth Surface*, 115(F1). <https://doi.org/10.1029/2009jf001302>

Erman, D., Status of the Sierra Nevada: Summary of the Sierra Nevada Ecosystem Project Report (1996). Davis, California; Centers for Water and Wildland Resources, University of California.

Ferdowsi, B., Ortiz, C. P., & Jerolmack, D. J. (2018). Glassy dynamics of landscape evolution. *Proceedings of the National Academy of Sciences*, 115(19), 4827–4832.
<https://doi.org/10.1073/pnas.1715250115>

Fernandes, N. F., & Dietrich, W. E. (1997). Hillslope evolution by diffusive processes: The timescale for equilibrium adjustments. *Water Resources Research*, 33(6), 1307–1318.
<https://doi.org/10.1029/97wr00534>

Foufoula-Georgiou, E., Ganti, V., & Dietrich, W. E. (2010). A nonlocal theory of sediment transport on Hillslopes. *Journal of Geophysical Research: Earth Surface*, 115(F2).
<https://doi.org/10.1029/2009jf001280>

Furbish, D. J., Hamner, K. K., Schmeeckle, M., Borosund, M. N., & Mudd, S. M. (2007). Rain splash of dry sand revealed by high-Speed Imaging and sticky paper splash targets. *Journal of Geophysical Research: Earth Surface*, 112(F1). <https://doi.org/10.1029/2006jf000498>

Furbish, D. J., Schmeeckle, M. W., & Roering, J. J. (2008). Thermal and force-chain effects in an experimental, sloping granular shear flow. *Earth Surface Processes and Landforms*, 33(13), 2108–2117. <https://doi.org/10.1002/esp.1655>

Furbish, D. J., Haff, P. K., Dietrich, W. E., & Heimsath, A. M. (2009). Statistical description of slope-dependent soil transport and the diffusion-like coefficient. *Journal of Geophysical Research: Earth Surface*, 114(F3). <https://doi.org/10.1029/2009jf001267>

Furbish, D. J., & Haff, P. K. (2010). From divots to swales: Hillslope sediment transport across divers length scales. *Journal of Geophysical Research: Earth Surface*, 115(F3).
<https://doi.org/10.1029/2009jf001576>

Furbish, D. J., Roering, J. J., Almond, P., & Doane, T. H. (2018a). Soil Particle Transport and mixing near a hillslope crest: 1. particle ages and residence times. *Journal of Geophysical Research: Earth Surface*, 123(5), 1052–1077. <https://doi.org/10.1029/2017jf004315>

Furbish, D. J., Roering, J. J., Keen-Zebert, A., Almond, P., Doane, T. H., & Schumer, R. (2018b). Soil Particle Transport and mixing near a hillslope crest: 2. Cosmogenic nuclide and Optically Stimulated Luminescence tracers. *Journal of Geophysical Research: Earth Surface*, 123(5), 1078–1093. <https://doi.org/10.1029/2017jf004316>

Furbish, D. J., Roering, J. J., Doane, T. H., Roth, D. L., Williams, S. G., & Abbott, A. M. (2021a). Rarefied particle motions on Hillslopes – Part 1: Theory. *Earth Surface Dynamics*, 9(3), 539–576. <https://doi.org/10.5194/esurf-9-539-2021>

- Furbish, D. J., Williams, S. G., Roth, D. L., Doane, T. H., & Roering, J. J. (2021b). Rarefied particle motions on Hillslopes – Part 2: Analysis. *Earth Surface Dynamics*, 9(3), 577–613. <https://doi.org/10.5194/esurf-9-577-2021>
- Furbish, D. J., Williams, S. G., & Doane, T. H. (2021c). Rarefied particle motions on hillslopes – part 3: Entropy. *Earth Surface Dynamics*, 9(3), 615–628. <https://doi.org/10.5194/esurf-9-615-2021>
- Furbish, D. J., & Doane, T. H. (2021d). Rarefied particle motions on Hillslopes – Part 4: Philosophy. *Earth Surface Dynamics*, 9(3), 629–664. <https://doi.org/10.5194/esurf-9-629-2021>
- Gabet, E. J. (2000). Gopher bioturbation: Field evidence for non-linear Hillslope Diffusion. *Earth Surface Processes and Landforms*, 25(13), 1419–1428. [https://doi.org/10.1002/1096-9837\(200012\)25:13<1419::aid-esp148>3.0.co;2-1](https://doi.org/10.1002/1096-9837(200012)25:13<1419::aid-esp148>3.0.co;2-1)
- Gabet, E. J., Reichman, O. J., & Seabloom, E. W. (2003). The effects of bioturbation on soil processes and sediment transport. *Annual Review of Earth and Planetary Sciences*, 31(1), 249–273. <https://doi.org/10.1146/annurev.earth.31.100901.141314>
- Gabet, E. J., & Mendoza, M. K. (2012). Particle transport over rough hillslope surfaces by dry Ravel: Experiments and simulations with implications for nonlocal sediment flux. *Journal of Geophysical Research: Earth Surface*, 117(F1). <https://doi.org/10.1029/2011jf002229>
- Ganti, V., Passalacqua, P., & Foufoula-Georgiou, E. (2012). A sub-grid scale closure for nonlinear hillslope sediment transport models. *Journal of Geophysical Research: Earth Surface*, 117(F2). <https://doi.org/10.1029/2011jf002181>
- Gago, P. A., & Boettcher, S. (2020). Universal features of annealing and aging in compaction of granular piles. *Proceedings of the National Academy of Sciences*, 117(52), 33072–33076. <https://doi.org/10.1073/pnas.2012757117>
- Gillespie, A. R., & Clark, D. H. (2011). Glaciations of the Sierra Nevada, California, USA. *Developments in Quaternary Sciences*, 447–462. <https://doi.org/10.1016/b978-0-444-53447-7.00034-9>
- Gonzalez De Vallejo, L. I., & Ferrer, M. (2011). *Geological Engineering*. CRC Press.
- Gray, H. J., Keen-Zebert, A., Furbish, D. J., Tucker, G. E., & Mahan, S. A. (2020). Depth-dependent soil mixing persists across climate zones. *Proceedings of the National Academy of Sciences*, 117(16), 8750–8756. <https://doi.org/10.1073/pnas.1914140117>
- Grieve, S. W. D., Mudd, S. M., & Hurst, M. D. (2016). How long is a Hillslope? *Earth Surface Processes and Landforms*, 41(8), 1039–1054. <https://doi.org/10.1002/esp.3884>

Hallet, B., & Putkonen, J. (1994). Surface dating of dynamic landforms: Young Boulders on aging moraines. *Science*, 265(5174), 937–940. <https://doi.org/10.1126/science.265.5174.937>

Hill, M., 2006, Geology of the Sierra Nevada: Berkeley, California, University of California Press, 453 p.

Heimsath, A. M., Chappell, J., Spooner, N. A., & Questiaux, D. G. (2002). Creeping soil. *Geology*, 30(2), 111. [https://doi.org/10.1130/0091-7613\(2002\)030<111:cs>2.0.co;2](https://doi.org/10.1130/0091-7613(2002)030<111:cs>2.0.co;2)

Heimsath, A. M., Furbish, D. J., & Dietrich, W. E. (2005). The illusion of diffusion: Field evidence for depth-dependent sediment transport. *Geology*, 33(12), 949. <https://doi.org/10.1130/g21868.1>

Henrique, C., Aguirre, M. A., Calvo, A., Ippolito, I., Dippel, S., Batrouni, G. G., & Bideau, D. (1998). Energy dissipation and trapping of particles moving on a rough surface. *Physical Review E*, 57(4), 4743–4750. <https://doi.org/10.1103/physreve.57.4743>

Houssais, M., & Jerolmack, D. J. (2017). Toward a unifying constitutive relation for sediment transport across environments. *Geomorphology*, 277, 251–264. <https://doi.org/10.1016/j.geomorph.2016.03.026>

Homer. (700 B.C.E.). *Odyssey*. a

Homer. (700 B.C.E.). *Iliad*. b

Hellmer, M. C., Rios, B. A., Ouimet, W. B., & Sibley, T. R. (2015). Ice storms, tree throw, and hillslope sediment transport in northern hardwood forests. *Earth Surface Processes and Landforms*, 40(7), 901–912. <https://doi.org/10.1002/esp.3690>

Hole, F. D. (1981). Effects of animals on soil. *Geoderma*, 25(1-2), 75–112. doi:10.1016/0016-7061(81)90008-2

Huber, N.K., 1981. Amount and timing of Cenozoic uplift and tilt of the central Sierra Nevada, California—evidence from the upper San Joaquin River. U.S. Geological Survey Professional Paper, 1197, 28pp

Jahn, A. (1991). Slow soil movement in Tarfala Valley, Kebnekaise Mountains, Swedish Lapland. *Geografiska Annaler. Series A, Physical Geography*, 73(2), 93. <https://doi.org/10.2307/520985>

Jaeger, H. M., & Nagel, S. R. (1992). Physics of the Granular State. *Science*, 255.

Jenny, H. (1941). *Factors of soil formation*. McGraw-Hill Book Co.

Jiang, F., Preisendanz, H. E., Veith, T. L., Cibin, R., & Drohan, P. J. (2020). Riparian buffer effectiveness as a function of buffer design and input loads. *Journal of Environmental Quality*, 49(6), 1599–1611. <https://doi.org/10.1002/jeq2.20149>

KIRCHNER, J. W., DIETRICH, W. E., ISEYA, F., & IKEDA, H. (1990). The variability of critical shear stress, friction angle, and grain protrusion in water-worked sediments. *Sedimentology*, 37(4), 647–672. <https://doi.org/10.1111/j.1365-3091.1990.tb00627.x>

Kirkby, A. V. T. and Kirkby, M. J. 1974. ‘Surface wash at the semi-arid break in slope’, *Zeitschriffrfur Geomorphologie Supplementband*, 21, 151-176.

Komatsu, T. S., Inagaki, S., Nakagawa, N., & Nasuno, S. (2001). Creep motion in a granular pile exhibiting steady surface flow. *Physical Review Letters*, 86(9), 1757–1760. <https://doi.org/10.1103/physrevlett.86.1757>

Krumbein, W. C., & Tisdel, F. W. (1940). Size distribution of source rocks of sediments. *American Journal of Science*, 238(4). <https://doi.org/10.2475/001c.57909>

Lal, D., 1991. Cosmic ray labeling of erosion surfaces in situ nuclide production rates and erosion models. *Earth and Planetary Science Letters* 104, 424-439.

Laurence, A. L. (1976): Soil movement in the tropics – a general model. - *Zeitschrift für Geomorphologie N. F. Suppl.-Bd 25*: 132 – 144.

Leopold, L. B., Emmett, W. W., Myrick, R. M. (1966). Channel and hillslope processes in a semiarid area, New Mexico. USGS Publications Warehouse. <https://pubs.usgs.gov/publication/pp352G>. DOI: 10.3133/pp352G

Louge, M. Y. (2003). Model for dense granular flows down bumpy inclines. *Physical Review E*, 67(6). <https://doi.org/10.1103/physreve.67.061303>

Mackay, J. R. (1981). Active layer slope movement in a continuous permafrost environment, Garry Island, Northwest Territories, Canada. *Canadian Journal of Earth Sciences*, 18(11), 1666–1680. <https://doi.org/10.1139/e81-154>

Madoff, Risa, "Climate Driven Hillslope Degradation Of Mono Basin Moraine, Eastern Sierra Nevada, California, USA" (2015). Theses and Dissertations. 1807.

Martin, Y., & Church, M. (1997). Diffusion in landscape development models: On the nature of basic transport relations. *Earth Surface Processes and Landforms*, 22(3), 273–279. [https://doi.org/10.1002/\(sici\)1096-9837\(199703\)22:3<273::aid-esp755&gt3.0.co;2-d](https://doi.org/10.1002/(sici)1096-9837(199703)22:3<273::aid-esp755>3.0.co;2-d)

Martin, Y. (2000). Modelling hillslope evolution: Linear and nonlinear transport relations. *Geomorphology*, 34(1–2), 1–21. [https://doi.org/10.1016/s0169-555x\(99\)00127-0](https://doi.org/10.1016/s0169-555x(99)00127-0)

- Matsuoka, N. (1998). The relationship between frost heave and downslope soil movement: Field Measurements in the Japanese Alps. *Permafrost and Periglacial Processes*, 9(2), 121–133. [https://doi.org/10.1002/\(sici\)1099-1530\(199804/06\)9:2<121::aid-ppp281>3.0.co;2-c](https://doi.org/10.1002/(sici)1099-1530(199804/06)9:2<121::aid-ppp281>3.0.co;2-c)
- McLaren, P., & Bowles, D. (1985). The effects of sediment transport on grain-size distributions. *SEPM Journal of Sedimentary Research, Vol. 55*. <https://doi.org/10.1306/212f86fc-2b24-11d7-8648000102c1865d>
- Moores, E.M., Sloan, D., and Stout, D.L., editors, 1999, Classic Cordilleran Concepts: A View from California: Boulder, CO, The Geological Society of America, 338, 489 p.
- New King James*. (1952). Thomas Nelson & Sons.
- Norman, S. A., Schaetzl, R. J., & Small, T. W. (1995). Effects of slope angle on mass movement by Tree uprooting. *Geomorphology*, 14(1), 19–27. [https://doi.org/10.1016/0169-555x\(95\)00016-x](https://doi.org/10.1016/0169-555x(95)00016-x)
- Oehm, B. & Hallet, B.. (2005). Rates of soil creep, worldwide: Weak climatic controls and potential feedback. *Zeitschrift fur Geomorphologie*. 49. 353-372.
- Phillips, F. M., Zreda, M. G., Smith, S. S., Elmore, D., Kubik, P. W., & Sharma, P. (1990). Cosmogenic chlorine-36 chronology for glacial deposits at Bloody Canyon, Eastern Sierra Nevada. *Science*, 248(4962), 1529–1532. <https://doi.org/10.1126/science.248.4962.1529>
- Phillips, F.M., Zreda, M.G., Benson, L.V., Plummer, M.A., Elmore, D., Sharma, P., 1996. Chronology for fluctuations in late Pleistocene Sierra Nevada glaciers. *Science* 274, 749–751.
- Phillips, F.M., Zreda, M., Plummer, M.A., Elmore, D., Clark, D.H., 2009. Glacial geology and chronology of Bishop Creek and vicinity, eastern Sierra Nevada, California. *Geol. Soc. Am. Bull.* 121, 1013–1033.
- Pommersheim, F. (1988). The Black Hills case: On the cusp of history. *Wicazo Sa Review*, 4(1), 18. <https://doi.org/10.2307/1409076>
- Persico, L. P., Nichols, K. K., & Bierman, P. R. (2005). Tracking painted pebbles: Short-term rates of sediment movement on four Mojave Desert Piedmont surfaces. *Water Resources Research*, 41(7). <https://doi.org/10.1029/2005wr003990>
- Pouliquen, O., & Forterre, Y. (2002). Friction law for dense granular flows: application to the motion of a mass down a rough inclined plane. *Journal of Fluid Mechanics*, 453, 133–151. <https://doi.org/10.1017/s0022112001006796>

Powell, J. W. (1879). *Report on the Land of the Arid Regions of the United States*. Government Printing Office.

Putkonen, J., & Swanson, T. (2003). Accuracy of Cosmogenic Ages for moraines. *Quaternary Research*, 59(2), 255–261. [https://doi.org/10.1016/s0033-5894\(03\)00006-1](https://doi.org/10.1016/s0033-5894(03)00006-1)

Putkonen, Jaakko, & O’Neal, M. (2006). Degradation of unconsolidated quaternary landforms in the western North America. *Geomorphology*, 75(3–4), 408–419. <https://doi.org/10.1016/j.geomorph.2005.07.024>

Putkonen, J., Rosales, M., Turpen, N., Morgan, D., Balco, G., & Donaldson, M. (2007). Regolith transport in the dry valleys of Antarctica. *USGS Special Open-File Report*. <https://doi.org/10.3133/ofr20071047srp103>

Putkonen, J., Rosales, M., Turpen, N., Morgan, D., Balco, G., & Donaldson, M. (2007). Regolith transport in the dry valleys of Antarctica. *USGS Special Open-File Report*. <https://doi.org/10.3133/ofr20071047srp103>

Putkonen, J., Connolly, J., & Orloff, T. (2008). Landscape evolution degrades the geologic signature of past glaciations. *Geomorphology*, 97(1–2), 208–217. <https://doi.org/10.1016/j.geomorph.2007.02.043>

Putkonen, J., Morgan, D. J., & Balco, G. (2012). Regolith transport quantified by braking block, McMurdo Dry Valleys, Antarctica. *Geomorphology*, 155–156, 80–87. <https://doi.org/10.1016/j.geomorph.2011.12.010>

Putkonen, J., Morgan, D., & Balco, G. (2014). Boulder weathering in McMurdo Dry Valleys, Antarctica. *Geomorphology*, 219, 192–199. <https://doi.org/10.1016/j.geomorph.2014.05.012>

Ritter, D. F., Kochel, R. C., & Miller, J. R. (2011). *Process geomorphology*. Waveland Press.

Roering, J. J., Kirchner, J. W., & Dietrich, W. E. (1999). Evidence for nonlinear, diffusive sediment transport on hillslopes and implications for landscape morphology. *Water Resources Research*, 35(3), 853–870. <https://doi.org/10.1029/1998wr900090>

Roering, J. J., Kirchner, J. W., & Dietrich, W. E. (2001). Hillslope evolution by nonlinear, slope-dependent transport: Steady State Morphology and Equilibrium Adjustment Timescales. *Journal of Geophysical Research: Solid Earth*, 106(B8), 16499–16513. <https://doi.org/10.1029/2001jb000323>

Roering, J. J., Perron, J. T., & Kirchner, J. W. (2007). Functional relationships between denudation and hillslope form and relief. *Earth and Planetary Science Letters*, 264(1–2), 245–258. <https://doi.org/10.1016/j.epsl.2007.09.035>

Roering, J. J. (2004). Soil creep and convex-upward velocity profiles: Theoretical and experimental investigation of disturbance-driven sediment transport on Hillslopes. *Earth Surface Processes and Landforms*, 29(13), 1597–1612. <https://doi.org/10.1002/esp.1112>

Rood, D.H., Burbank, D.W., and Finkel, R.C., 2011, Chronology of glaciations in the Sierra Nevada, California, from 10Be surface exposure dating: Quaternary Science Reviews, v. 30, no. 6, p. 646-661.

Rose, N. L., Morley, D., Appleby, P. G., Battarbee, R. W., Alliksaar, T., Guilizzoni, P., Jeppesen, E., Korhola, A., & Punning, J.-M. (2010). Sediment accumulation rates in European lakes since AD 1850: Trends, reference conditions and exceedence. *Journal of Paleolimnology*, 45(4), 447–468. <https://doi.org/10.1007/s10933-010-9424-6>

Roth, D. L., Doane, T. H., Roering, J. J., Furbish, D. J., & Zettler-Mann, A. (2020). Particle motion on burned and vegetated hillslopes. *Proceedings of the National Academy of Sciences*, 117(41), 25335–25343. <https://doi.org/10.1073/pnas.1922495117>

Sklar, L. S., Riebe, C. S., Marshall, J. A., Genetti, J., Leclere, S., Lukens, C. L., & Merces, V. (2017). The problem of predicting the size distribution of sediment supplied by hillslopes to Rivers. *Geomorphology*, 277, 31–49. <https://doi.org/10.1016/j.geomorph.2016.05.005>

Smith, Dan. (1988). Rates and controls of soil movement on a solifluction slope in the Mount Rae area, Canadian Rocky Mountains. *Zeitschrift fur Geomorphologie*, N.F. Suppl. Bd.. 71. 25-44.

Staron, L. (2008). Correlated motion in the bulk of dense granular flows. *Physical Review E*, 77(5). <https://doi.org/10.1103/physreve.77.051304>

Stine, S., 1994. Extreme and persistent drought in California and Patagonia during mediaeval time. *Nature* 369, 546–549.

Thorn, C. E., Dixon, J. C., Darmody, R. G., & Allen, C. E. (2006). A 10-year record of the weathering rates of surficial pebbles in Kärkevagge, Swedish Lapland. *CATENA*, 65(3), 272–278. <https://doi.org/10.1016/j.catena.2005.12.002>

Tucker, G. E., & Bradley, D. N. (2010). Trouble with diffusion: Reassessing hillslope erosion laws with a particle-based model. *Journal of Geophysical Research: Earth Surface*, 115(F1). <https://doi.org/10.1029/2009jf001264>

US Department of Commerce, N. (2024, December 16). *Climate*. National Weather Service. <https://www.weather.gov/wrh/climate?wfo=rev>

Van, A. (1945). Angle of Repose and Angle of Sliding Friction: An Experimental Study. *Geological Society of America Bulletin*, 56(6), 669–708. [https://doi.org/10.1130/0016-7606\(1945\)56\[669:AORAAO\]2.0.CO;2](https://doi.org/10.1130/0016-7606(1945)56[669:AORAAO]2.0.CO;2)

- Vasquez, T. (2009). *Severe storm forecasting*. Weather Graphics Technologies.
- Wiberg, P. L., & Smith, J. D. (1987). Calculations of the critical shear stress for motion of uniform and heterogeneous sediments. *Water Resources Research*, 23(8), 1471–1480. <https://doi.org/10.1029/wr023i008p01471>
- White, A. F., & Brantley, S. L. (2003). The effect of time on the weathering of silicate minerals: Why do weathering rates differ in the laboratory and field? *Chemical Geology*, 202(3–4), 479–506. <https://doi.org/10.1016/j.chemgeo.2003.03.001>
- Williams, H., Coats, R. R., Hay, R. L., & Anderson, C. A. (1968). *Studies in Volcanology: A memoir in honor of Howel Williams. Robert R. Coats, Richard L. Hay, and Charles A. Anderson, editors*. Geological Society of America.
- Williams, S. G., & Furbish, D. J. (2021). Particle energy partitioning and transverse diffusion during rarefied travel on an experimental hillslope. *Earth Surface Dynamics*, 9(4), 701–721. <https://doi.org/10.5194/esurf-9-701-2021>
- Wells, Wade G., II, Wohlgemuth, PeterM. Sediment traps for measuring onslope surface sediment movement. Res. Note PSW-393. Berkeley, CA: Pacific Southwest Forest and Range Experiment Station, Forest Service, U.S. Department of Agriculture; 1987. 6 p.
- Wuenscher, Timothy, "Regolith Transport Rates And Grain Size Distributions On Hillslopes, Sierra Nevada, Ca" (2018). Theses and Dissertations. 2438.

Appendix

Soil surface grain transport data

Sample #	Distance from origin (mm)	1.981mm	0.589-1.0mm
2021-BC-GT-1	-9.5	0	0
	0	26	54
	9.5	14	123
	19	0	5
	28.5	0	0
	38	0	0
	47.5	0	0
Slope angle: 18 degrees			
	Total recovered	40	182
	Avg displacement (cm)	3.325	6.942307692
	Total placed in field	255	3250
	Recovery %	15.68627	17.78

Sample #	Distance from origin (mm)	1.981mm	0.589-1.0mm
2021-BC-GT-3	-9.5	0	0
	0	4	4
	9.5	9	341
	19	70	12
	28.5	32	0
	38	8	0
	47.5	0	8
Slope angle: 25 degrees			
	Total recovered	40	182
	Avg displacement (cm)	65.7875	21.14010989
	Total placed in field	255	3250
	Recovery %	25.79902	17.78

Sample #	Distance from origin (mm)	1.981mm	0.589-1.0mm
2021-BC-GT-4	-9.5	14	9
	0	94	98
	9.5	22	6

	19	0	0
	28.5	0	0
	38	5	5
	47.5	0	0
Angle: 23 degrees	Total recovered	40	182
	Avg displacement (cm)	13.3	1.826923077
	Total placed in field	255	3250
	Recovery %	5.215686	17.78

Distance from origin (mm)		1.981mm	0.589-1.0mm
2021-BC-GT-7	-9.5	0	0
	0	90	238
	9.5	8	8
	19	0	5
	28.5	0	4
	38	0	4
	47.5	0	0
Angle: 23 degrees	Total recovered	40	182
	Avg displacement (cm)	1.9	2.401098901
	Total placed in field	255	3250
	Recovery %	15.68627	17.78

Distance from origin (mm)			
2021-BC-GT-8	-9.5	0	0
	0	140	498
	9.5	80	25
	19	20	7
	28.5	8	0
	38	0	0
Angle: 27 degrees	47.5	0	0
	Total recovered	40	182
	Avg displacement (cm)	34.2	2.035714286
	Total placed in field	255	3250
	Recovery %	13.41176	17.78

		Distance from origin	
Sample #	(mm)	1.981mm	0.589-1.0mm
2021-SC-GT-1	-4.25 to -13.75	0	225
	-4.25 to 4.25	4	240
	4.25 to 13.75	0	15
	13.75 to 23.25	10	250
	23.25 to 32.75	0	0
	32.75 to 42.25	0	5
Angle: 10 degrees	42.25 to 51.75	0	0
	Total recovered	14	735
	Avg displacement	13.21428571	9.234693878
	Total placed in field	1000	5000
	Recovery %	1.4	14.7

		Distance from origin	
Sample #	(mm)	1.981mm	0.589-1.0mm
2021-SC-GT-2	-23.25 to -32.75	5	0
	-13.75 to -23.25	0	0
	-4.25 to -13.75	4	0
	-4.25 to 4.25	0	27
	4.25 to 13.75	7	343
	13.75 to 23.25	0	78
Angle: 11.2 degrees	23.25 to 32.75	0	15
	32.75 to 42.25	0	0
	42.25 to 51.75	0	0
	Total recovered	16	463
	Avg displacement	6.75	10.69114471
Angle: 11.2 degrees	Total placed in field	1000	5000
	Recovery %	1.6	9.26

		Distance from origin	
Sample #	(mm)	1.981mm	0.589-1.0mm
2021-SC-GT-3	-4.25 to -13.75	15	310
	-4.25 to 4.25	400	775
	4.25 to 13.75	15	90
	13.75 to 23.25	0	8
	23.25 to 32.75	3	9
	32.75 to 42.25	0	0
Angle: 10 degrees	42.25 to 51.75	0	0
	Total recovered	433	1192
	Avg displacement	0.817551963	0.039848993

Total placed in field	1000	5000
Recovery %	43.3	23.84

Distance from origin (mm)		1.981mm	0.589-1.0mm
Sample # 2021-SC-GT-4	-4.25 to -13.75	9	60
	-4.25 to 4.25	432	2880
	4.25 to 13.75	7	56
	13.75 to 23.25	0	0
	23.25 to 32.75	0	0
	32.75 to 42.25	0	0
	42.25 to 51.75	0	0
Total recovered		448	2996
Angle: 9.5 degrees	Avg displacement	0.321428571	0.044392523
	Total placed in field	1000	5000
	Recovery %	44.8	59.92

Distance from origin (mm)		1.981mm	0.589-1.0mm
Sample # 2021-SC-GT-5	-4.25 to -13.75	0	7
	-4.25 to 4.25	0	90
	4.25 to 13.75	84	378
	13.75 to 23.25	0	21
	23.25 to 32.75	8	24
	32.75 to 42.25	0	0
	42.25 to 51.75	0	0
Angle: 9 degrees	Total recovered	92	520
	Avg displacement	10.65217391	8.702884615
	Total placed in field	1000	5000
	Recovery %	9.2	10.4

Distance from origin (mm)		1.981mm	0.589-1.0mm
Sample # 2021-SC-GT-6	-4.25 to -13.75	0	36
	-4.25 to 4.25	0	186
	4.25 to 13.75	0	1200
	13.75 to 23.25	3	69
	23.25 to 32.75	0	7
	32.75 to 42.25	0	0

Angle: 8 degrees	42.25 to 51.75	0	0
	Total recovered	3	1498
	Avg displacement	18.5	8.408878505
	Total placed in field	1000	5000
	Recovery %	0.3	29.96

Sample #	Distance from origin (cm)	0.589-	
		1.981mm	1.0mm
2022-SC-GT-1	-28.5	0	0
	-19	0	0
	-9.5	0	36
	0	0	720
	9.5	0	98
	19	0	35
	28.5	0	0
	38	0	0
	47.5	0	0
	57	0	0
Angle: 18 degrees	100	0	0
	Total recovered	0	889
	Avg displacement (cm)	#DIV/0!	2.179977503
	Total placed in field	255	3250
	Recovery %	0	17.78

Sample #	Distance from origin (mm)	0.589-	
		1.981mm	1.0mm
2022-SC-GT-2	-28.5	0	0
	-19	12	6
	-9.5	0	16
	0	150	1950
	9.5	25	45
	19	0	3
	28.5	0	0
	38	0	0
	47.5	0	0
	57	0	0
Angle: 9 degrees	100	0	0
	Total recovered	187	2020
	Ave displacement (cm)	2.489305	0.371534653
	Total placed in field	247	3125
	Recovery %	75.7085	40.4

0.589 -			
	Distance from origin (mm)	1.981	1.0mm
	-28.5	0	0
	-19	0	0
	-9.5	0	0
	0	20	560
Sample #	9.5	40	360
2022-SC-GT-3	19	7	40
	28.5	10	16
	38	3	3
	47.5	6	12
	57	0	0
Angle: 20 degrees	100	3	6
	Total recovered	89	997
	Avg displacement	16.82022	5.93781344
	Total placed in field	240	3125
	Recovery %	29.66667	19.94

0.589-			
	Distance from origin (mm)	1.981mm	1.0mm
	-28.5	0	0
Sample #	-19	0	0
2022-SC-GT-4	-9.5	0	126
	0	30	1100
	9.5	5	36
	19	0	6
	28.5	0	3
	38	0	0
	47.5	0	3
	57	0	0
Angle: 20 degrees	100	3	4
	Total recovered	38	1278
	Avg displacement	9.144737	1.784820031
	Total placed in field	247	3125
	Recovery %	12.66667	25.56

0.589-			
	Distance from origin (mm)	1.981mm	1.0mm
	-28.5	0	4
Sample #	-19	0	13
2022-SC-GT-5	-9.5	8	88

Heavily bioturbated by elodeous beetle	0	0	444
	9.5	0	200
	19	0	68
	28.5	0	2
	38	0	3
	47.5	0	0
	57	0	0
	100	0	0
Angle: 21 degrees	Total recovered	8	822
	Avg displacement	9.5	5.547445255
	total placed in field	231	3125
	Recovery %	3.463203	26.304

	Distance from origin (mm)	1.981mm	0.589-1.0mm
Sample #	-28.5	0	0
2022-SC-GT-6	-19	0	0
Heavily bioturbated by elodeous beetle	-9.5	0	3
	0	85	500
	9.5	15	210
	19	2	6
Angle: 19 degrees	28.5	0	0
	38	0	0
	47.5	0	0
	57	0	0
	100	0	0
	Total recovered	102	719
	Avg displacement	1.769608	2.972878999
	Total placed in field	247	3125
	Recovery %	41.29555	23.008

Sample #	Distance from origin (cm)	2mm	0.75 mm
2023-BC-SGT-1	-28.5	0	0
	-19	0	0
	-9.5	0	0
	0	0	25
	9.5	54	120
	19	6	18
	28.5	28	18
	38	21	12

	47.5	2	29
Angle: 20 degrees	57	0	0
	66.5	2	5
	76	0	4
	100	0	0
Total recovered	113	231	
Avg displacement (cm)	21.69027	19.32900433	
Total placed in field	500	3000	
Recovery %	22.6	7.7	

Sample #	Distance from origin (cm)	2mm	0.75 mm
	-28.5	0	0
	-19	0	0
	-9.5	0	0
	0	0	444
2023-BS-SGT-2	9.5	5	30
	19	3	5
	28.5	3	3
	38	3	0
	47.5	0	0
Angle: 20 degrees	57	0	0
	66.5	0	0
	76	0	0
	100	0	0
Total recovered	14	482	
Avg displacement (cm)	21.71429	0.965767635	
Total placed in field	500	3200	
Recovery %	2.8	15.0625	

Sample #	Distance from origin (cm)	2mm	0.75 mm
	-28.5	0	0
	-19	0	0
	-9.5	0	0
	0	0	34
2023-BS-SGT-3	9.5	7	160
	19	38	315
	28.5	44	48
	38	42	30

	47.5	8	20
Angle: 20 degrees	57	4	8
	66.5	0	3
	76	0	0
	100	0	0
Total recovered	143	618	
Avg displacement (cm)	29.6958	18.80016181	
Total placed in field	500	2500	
Recovery %	28.6	24.72	

Sample #	Distance from origin (cm)	2mm	0.75 mm
	-28.5	0	0
	-19	0	0
	-9.5	0	0
	0	0	34
2023-BS-SGT-4	9.5	186	560
	19	16	20
	28.5	11	4
	38	4	0
	47.5	0	0
Angle: 20 degrees	57	0	0
	66.5	0	0
	76	0	0
	100	0	0
Total recovered	217	618	
Avg displacement (cm)	11.68894	9.40776699	
Total placed in field	500	2500	
Recovery %	43.4	24.72	

Sample #	Distance from origin (cm)	2mm	0.75 mm
	-28.5	0	0
	-19	0	0
	-9.5	0	0
	0	4	0
2023-BS-SGT-5	9.5	0	4
	19	8	36
	28.5	56	680
	38	48	112
	47.5	8	112
Angle: 20 degrees	57	3	0
	66.5	0	0

	76	0	0
	100	0	0
Total recovered		127	944
Avg displacement (cm)		32.46457	31.43855932
Total placed in field		500	1100
Recovery %		25.4	85.81818182

Sample #	Distance from origin (cm)	2mm	0.75 mm
		-28.5	0
2023-BS-SGT-6	-19	0	0
	-9.5	0	0
	0	0	12
	9.5	39	300
	19	48	210
	28.5	7	5
	38	0	0
Angle: 18 degrees	47.5	0	0
	57	0	0
	66.5	0	0
	76	0	0
	100	0	0
Total recovered		94	527
Avg displacement (cm)		15.76596	13.24952562
Total placed in field		500	2300
Recovery %		18.8	22.91304348

30 mm pebble surface transport data

2021 - SC-PB -	Pebble	Transport distance
2	1	1.8
	2	10
	3	21
	4	24
	5	1
	6	8.5
	7	15
	8	3.5
	9	2
	10	3.15

11	3.15
12	4.12
13	11.1
14	0
15	2
16	1.3
17	4
18	4
19	5.4
Mean =	6.58

2021-SC-PB-1	Pebble	Transport distance
	1	0
	2	1
	3	2
	4	0
	5	8.2
	6	3.5
	7	1
	8	0
	9	0
	10	0
	11	0
	12	2
	13	0
Mean =		1.361538462

2022-sc-pb-2	pebble	transport distance
	1	2
	2	2
	3	7
	4	6
	5	11
	6	7
	7	6
	8	-1
	9	5
	10	8
	11	1
	12	0

13	0
14	0
15	0
16	0
17	8
18	0
mean =	3.444444444

Mobile Layer data

Color Initial Depth (number indicates lower bound in cm)

Black	1
Silver	2
Purple	3
Blue	4
White	5
Bismuth	6

2022-sc-ml-1	Color	Post depth min (cm)	Post depth max (cm)	Depth of minimum transport (cm)	Min transport distance (cm)	depth of maximum transport (cm)	max transport distance (cm)
	Black	2	5	2	2	5	2
	Silver	3	6	3	2	6	2
	Purple	4	8	4	2	8	2
	Blue	5	9	5	2	9	2
	White	7	9	7	2	9	2
	Bismuth	8	11	8	2	11	2

2022-sc-ml-2	Color	Post depth min	Post depth max	Depth of minimum transport (cm)	Min transport distance (cm)	depth of maximum transport (cm)	max transport distance (cm)
	Black	0	0	0	0	0	30
	Silver	0	0	0	0	0	30
	Purple	0	2	2	2	0	26
	Blue	2	4	4	2	2	2
	White	4	5	5	1	4	2
	Bismuth	5	6	6	0	5	1

2022-sc-ml-3	Color	Post	Post	Depth of	Min transport	depth of	max transport
		depth	depth	minimum		maximum	
		min	max	transport (cm)		transport (cm)	distance (cm)
	Black	0	4	4	0	0 > 100	
	Silver	0	4	4	0	0 > 100	
	Purple	0	4	4	0	0 > 100	
	Blue	0	4.25	4.25	2	0	70
	White	4	5	5	1	4	2
	Bismuth	5	6.5	6.5	0	5	1

2022-sc-ml-4	Color	Post	Post	Depth of	Min transport	depth of	max transport
		depth	depth	minimum		maximum	
		min	max	transport (cm)		transport (cm)	distance (cm)
	Black	0	0	0	0	0 > 100	
	Silver	0	1	1	5	0	51
	Purple	0.75	2	2	3	0.75	5
	Blue	2	3	3	2	2	3
	White	3	5	5	0	3	2
	Bismuth	5	6	6	0	5	0

2022-sc-ml-5	Color	Post	Post	Depth of	Min transport	depth of	max transport
		depth	depth	minimum		maximum	
		min	max	transport (cm)		transport (cm)	distance (cm)

Black	0.5	3	3	0.5	0.5	1
Silver	0.5	3	3	0.5	0.5	1
Purple	2.5	5	5	0	2.5	1
Blue	4	5	5	0	4	0.5
White	5	6.5	6.5	0	5	0
Bismuth	5	7	7	0	5	0

2023-bc-ml-1	Color	Post	Post	Depth of	Min transport distance (cm)	depth of maximum transport (cm)	max transport distance (cm)
		depth min	depth max	minimum transport (cm)			
	Black	0	2.5	2.5	1	0	4
	Silver	0	3	3	0.5	0	12.7
	Purple	3	4.25	4.25	0.5	3	2
	Blue	3	5	5	0	3	1
	White	4.25	6.5	6.5	0	4.25	0
	Bismuth	5.5	7.5	7.5	0	7.5	0

2023-bc-ml-2	Color	Post	Post	Depth of	Min transport distance (cm)	depth of maximum transport (cm)	max transport distance (cm)
		depth min	depth max	minimum transport (cm)			
	Black	2.5	4.5	4.5	1	2.5	8
	Silver	3	4.5	4.5	1	3	8
	Purple	3.5	5	5	1	3.5	8
	Blue	4	5.5	5.5	1	4	3
	White	5	6.5	6.5	0	5	0
	Bismuth	6	7.5	7.5	0	6	0

2023-bc-ml-3	Color	Post	Post	Depth of	Min	depth of	max transport
		depth min	depth max	minimum transport (cm)	transport distance (cm)		
	Black	0	3.5	3.5	10	0	200
	Silver	0	2	2	5	0	127
	Purple	0	2	2	3	0	167
	Blue	0	6	6	2	0	76
	White	3	6	6	0	3	6
	Bismuth	4.5	7.5	7.5	0	4.5	4

2023-bc-ml-4	Color	Post	Post	Depth of	Min	depth of	max transport
		depth min	depth max	minimum transport (cm)	transport distance (cm)		
	Black	0	2	2	6	0	48
	Silver	0	3	3	3	0.5	6
	Purple	1	4	4	1	1	4
	Blue	3.5	5	5	0	3.5	2
	White	4.25	6	6	0	4.25	1
	Bismuth	5	7	7	0	5	0

2023-bc-ml-5	Color	Post	Post	Depth of	Min transport distance (cm)	depth of maximum transport (cm)	max transport distance (cm)
		depth min	depth max	minimum transport (cm)			
	Black	0	2	2	6	0	43
	Silver	0	3.5	3.5	4	0	9
	Purple	2	3.5	3.5	4	2	9
	Blue	2.5	4	4	2	2.5	8
	White	3.5	5	5	2	3.5	5
	Bismuth	4.5	7	7	0	4.5	2

2023-bc-ml-6	Color	Post	Post	Depth of	Min transport distance (cm)	depth of maximum transport (cm)	max transport distance (cm)
		depth min	depth max	minimum transport (cm)			
	Black	0	0	0	0	0	0
	Silver	0	2	2	12	0	175
	Purple	0	3	3	8	0	112
	Blue	2	4	4	4	2	9
	White	3.5	6	6	3	3.5	7
	Bismuth	5	7.5	7.5	0	5	2

Random Grain Transport Model Inputs

	2 mm - 5 degrees	2 mm - 10 degrees	2 mm - 15 degrees	2 mm - 20 degrees	2 mm - 25 degrees
num_stationary	0.29			0.14	0.04
radial	0.95	0.95		0.95	0.95
downslope	0.05	0.05		0.05	0.05
probability	0.0001	0.001		0.67	0.8
Move probability	0.0001	0.001		0.01	0.01
Radial Downslope bias	0.05	0.05		0.05	0.05
Total Transport distance	15.5	16.4		17	18.6
					19.3

0.75 mm - 5 degrees	0.75 mm - 10 degrees	0.75 mm - 15 degrees	0.75 mm - 20 degrees	0.75 mm - 25 degrees
0.28	0.2	0.15	0.15	0.15
0.97	0.97	0.97	0.97	0.97
0.03	0.03	0.03	0.03	0.03
0.0001	0.001	0.01	0.01	0.01
0.0001	0.001	0.001	0.001	0.001
0.05	0.05	0.05	0.05	0.05
15.4	15.8	16.05	16.8	17.1

2 mm particles		0.75 mm particles	
elevation	distance	elevation	distance
5	15.6	5	15.4
10	16.4	10	15.8
15	17	15	16.05
20	18.6	20	16.8
25	19.3	25	17.1
average	16.9	average	16.1

Random Grain Transport Model Results:

Weather & Climate Data for Lee Vining, CA (* indicates study period):

Precipitation (Meters):

Year	January	February	March	April	May	June	July	August	September	October	November	December	Annual
1994	0.01	0.27	0.03	0.01	0.09	0	0	0	0.02	0.06	0.1	0.01	0.05
1995	0.26	0.02	0.32	0.01	0.03	0.03	0	0	T	0	0	0.11	0.07
1996	0.14	0.19	0.02	0.04	0.02	T	0.04	0.02	0	0.07	0.2	0.2	0.08
1997	0.24	0.01	T	T	T	0.03	0.05	0.02	0.01	0	M	0.03	0.04
1998	0.05	0.3	0.07	M	T	M	0	T	0.04	0.01	M	0.01	0.05
1999	0.09	0.11	M	0.04	T	0	0	0.01	0.01	0.01	0.02	0	0.03
2000	0.09	0.11	0.03	0.01	0.01	0	0	0.03	0	0.02	0.01	0.02	0.03
2001	0.05	0.08	M	0.05	0	0	0.03	0.02	M	0.01	0.06	M	0.03
2002	0.01	M	0.04	0.01	0	0	0.03	T	0.02	0	0.13	0.16	0.04
2003	0	0.06	0.03	0.04	0.02	0.01	0.01	0.03	0.02	0	0.03	0.08	0.03
2004	0.07	0.12	0.01	T	0.02	0.01	0.02	0.03	0	0.07	0.08	0.11	0.05
2005	0.18	0.09	0.08	M	0.03	0	0	0.03	0.02	0.01	0.02	M	0.05
2006	0.18	0.08	0.06	0.08	0.03	0.01	0.01	0	T	0.03	0.01	0.04	0.04
2007	0.02	0.07	0.01	0.01	0	0	0.01	0.04	0.01	0	0.01	M	0.02
2008	M	0.08	0.01	0	0.04	0	0	0	T	0.01	0.05	0.05	0.02
2009	0.03	M	0.07	0.01	0.03	0.03	0	0.01	T	0.08	0.02	0.06	0.03
2010	0.12	0.12	0.02	0.06	0.01	T	0.01	T	0	0.12	0.07	0.26	0.07
2011	0.02	0.09	0.13	0.02	0.01	0.03	0.01	0	0.01	0.04	0.01	T	0.03
2012	0.08	0.01	0.04	0.01	T	0	0	0.02	0	0.03	0.03	0.16	0.03
2013	0.01	T	0	0.01	0.03	0	0.03	0.02	0.02	0.02	0.01	0.02	0.01
2014	0.04	0.07	0.04	0.02	0.01	0.02	0.03	0.03	0.03	0	0.02	0.03	0.03
2015	0.01	0.04	0.02	0.02	0.13	0.02	0.07	0	0.01	0.04	0.04	0.05	0.04
2016	0.08	0.04	0.04	0.04	0.03	0.04	0.02	0	0.03	0.07	0.02	0.07	0.04

2017	0.36	0.23	0.04	0.06	0.03	0	0	0.02	0.02	0	0.09	T	0.07
2018	0.02	0.01	0.12	0.04	0.08	0	0.06	0	T	0.01	0.07	0.02	0.04
2019	0.09	0.21	0.08	0	0.03	0.01	0.02	0	0	0	0.03	0.06	0.04
2020	0.02	T	0.05	0.07	0.01	0.01	0.01	0.02	0	0	0.04	0.04	0.02
2021*	0.13	0.02	0.01	0	0.01	0.02	0.06	T	0	0.08	0	0.2	0.04
2022*	0	0	M	0	M	T	0	0.05	0.02	0	0.06	0.18	0.03
2023*	0.33	0.16	0.21	T	0	0.02	0	0.03	0.01	0.02	0.02	0.01	0.07
2024*	0.04	0.2	0.08	0.01	0.01	0	0.02	T	0.01	0.01	0.03	0.05	0.04
Mean	0.09	0.1	0.06	0.02	0.02	0.01	0.02	0.01	0.01	0.03	0.04	0.07	0.48
Max	0.36	0.3	0.32	0.08	0.13	0.04	0.07	0.05	0.04	0.12	0.2	0.26	0.08
Min	0	T	T	0	0	0	0	0	0	0	0	0	0.01
	2017	1998	1995	2006	2015	2016	2015	2022	1998	2010	1996	2010	
	2022	2020	1997	2008	2001	2018	2022	2019	2010	2020	2021	1999	

M = Missing, T = Trace

Anomaly:

2021	0.04	-0.08	-0.05	-0	-0	0.01	0.04	T	-0.01	0.05	-0.04	0.13	0
2022	-0.09	-0.1	M	-0	M	T	-0	0.04	0.01	-0.03	0.02	0.11	-0.01
2023	0.24	0.06	0.15	T	-0	0.01	-0	0.02	0	-0.01	-0.02	-0.06	0.03
2024	-0.05	0.1	0.02	-0	-0	-0.01	0	T	0	-0.02	-0.01	-0.02	0

Average Temperature (Deg. F):

Year	January	February	March	April	May	June	July	August	September	October	November	December	Annual
1994	33.1	30.7	42.8	46.8	53.3	64.8	71.1	69.9	60.3	47.6	31.3	30.3	48.5
1995	29.6	36.8	35.6	43.3	48.4	56.5	66	67.4	62.3	52.7	47	34.7	48.4
1996	36.1	34.9	38.5	46.2	53.6	61.7	70	67.4	59.6	50	39	35.9	49.4
1997	29.4	33.6	45	M	56.9	60.3	64.7	66.9	M	49.6	M	27.7	48.2
1998	31.9	M	35.7	40.8	46.4	M	68.1	69.2	58.1	46.7	M	M	49.6
1999	33.4	33.1	M	M	52.8	61.9	67.8	64.6	60.5	54.2	45.2	34.8	50.8
2000	35.9	35.5	40.1	48	57.1	64.3	67.4	67.5	60	49.3	36.4	36.1	49.8
2001	27.4	28	41.3	43.2	59.2	64.7	67.1	69.8	63.3	55.1	41.9	30.9	49.3
2002	31	37.3	37.5	47	51.9	64.8	71.4	66.7	61.3	49.2	40.4	31.5	49.2
2003	30.1	31.8	41	41.6	53.5	64.6	70.9	67.4	62.4	56.1	37	32.8	49.1
2004	32.1	29.8	44.7	M	M	63	68.6	65.4	59.8	47	36.3	32.1	47.9
2005	23.6	30.2	36.6	42.5	53.5	58	71.4	67	56.6	50.4	42.6	34.3	47.2
2006	27	M	M	43.2	55.2	64.6	71.1	65.5	59.3	47.6	41.9	31.2	50.7
2007	28	35.3	45.6	47.1	55.9	64.4	72.3	69.1	58.9	49	M	M	52.6
2008	26.5	27.7	37.5	46.5	51.4	62.5	70.8	70.1	61.1	49.4	42.2	30.4	48
2009	33.4	32.4	38.1	44	57.8	58.1	69.7	65.8	63.4	47.1	40.9	26	48.1
2010	28.8	31.6	36.9	40.5	46.6	61.8	69.5	66.7	61.5	50.1	38.3	M	48.4
2011	27.8	29.7	36.8	43.7	47.6	58.8	67.7	69	63.5	51.8	38.2	30.2	47.1
2012	35.7	34	39.7	49.6	55.5	63.7	70.3	70.7	64.4	53	43.1	33.2	51.1
2013	21.7	32.9	43.8	47.4	54.2	65.2	70.7	67	59.7	46.6	41	30.7	48.4
2014	36.8	38.5	40.8	47	54.6	63.9	70.4	65.9	62.7	55	43.9	35.5	51.2
2015	37.6	42.8	46	46.3	50.1	65.4	65.4	68.6	63.6	53.3	36.3	31.5	50.6
2016	32.8	39.5	43.5	48.1	51	64.9	69.5	68.9	60	51.4	42.5	34.5	50.6
2017	25.9	34.5	42.9	45.8	54.8	64.5	71.3	69.1	58.4	49.4	46.1	35	49.8
2018	38.3	34.1	36.2	48.1	53.5	65.2	71.8	68.7	62.5	48.5	41.4	32	50

2019	32.8	27.1	36	48.7	49.1	61.4	68.2	69.4	59.7	46.9	40.8	32.3	47.7
2020	35.5	37.2	36.6	46.3	55.5	61.1	69.7	68.6	63.1	53.5	39.6	32.9	50
2021*	32	31.9	37.1	47.4	54.5	67.5	72.3	69.3	63.3	46.5	44.6	31.7	49.8
2022*	31	33.3	41.6	45.9	51.3	62.2	71.8	69.6	63.7	52	30.9	29.2	48.5
2023*	22.7	21.6	28.1	41.5	53.4	57.8	71.9	67.1	60.1	50.4	39.6	36.3	45.9
2024*	33.8	31.2	37.6	46.6	53.9	67.4	72.5	68.9	62.2	54.3	36.8	35.9	50.1
Mean	31	33	39.4	45.5	53.1	62.8	69.7	68	61.2	50.4	40.2	32.5	49.2
Max	38.3 2018	42.8 2015	46 2015	49.6 2012	59.2 2001	67.5 2021	72.5 2024	70.7 2012	64.4 2012	56.1 2003	47 1995	36.3 2023	52.6
Min	21.7 2013	21.6 2023	28.1 2023	40.5 2010	46.4 1998	56.5 1995	64.7 1997	64.6 1999	56.6 2005	46.5 2021	30.9 2022	26 2009	45.9

Anomaly:

2021	1	-1.1	-2.3	1.9	1.4	4.7	2.6	1.3	2.1	-3.9	4.4	-0.8	0.6
2022	0	0.3	2.2	0.4	1.8	-0.6	2.1	1.6	2.5	1.6	-9.3	-3.3	-0.7
2023	-8.3	-11.4	-11.3	-4	0.3	-5	2.2	-0.9	-1.1	0	-0.6	3.8	-3.3
2024	2.8	-1.8	-1.8	1.1	0.8	4.6	2.8	0.9	1	3.9	-3.4	3.4	0.9

Snow depths (inches):

Year	July	August	September	October	November	December	January	February	March	April	May	June	Annual
1993-1994	0	0	M	0	M	M	0.3	M	M	0	M	0	0
1994-1995	0	0	0	0	M	M	M	M	M	0	0	M	0
1995-1996	0	0	0	0	0	M	M	M	M	M	0	0	0
1996-1997	0	0	0	0.9	M	M	M	M	0	0	0	0	0.1
1997-1998	0	0	0	0	M	M	M	M	M	M	0	M	0
1998-1999	0	0	0	M	0	0	M	M	M	M	0	0	0
1999-2000	0	0	0	0	0	0	M	0.1	M	0	0	0	0
2000-2001	0	0	0	0	M	0	M	10.2	M	M	0	0	1.3
2001-2002	0	0	0	0	0.8	M	M	M	0.5	M	0	0	0.2
2002-2003	0	0	0	0	0	M	15	3.3	0.6	M	0	0	1.9
2003-2004	0	0	0	0	M	M	M	5.6	M	0	0	0	0.7
2004-2005	0	0	0	0.8	0.7	M	M	19.7	5	M	0	0	2.9
2005-2006	0	0	0	0	0	M	20.5	1.5	0.7	0.1	0	0	2.1
2006-2007	0	0	0	0	0	M	0.5	0.8	0.3	M	0	0	0.2
2007-2008	0	0	0	M	0	M	13.6	M	2	0	0	0	1.7
2008-2009	0	0	0	0.1	M	2.2	0.8	5	1.2	0	0	0	0.8
2009-2010	0	0	0	0.1	0.2	M	M	9.6	2.4	0.7	0.1	0	1.3
2010-2011	0	0	0	0	1.6	M	M	4.6	5.2	0.1	0.1	0	1.2
2011-2012	0	0	0	0	0	0	1	0.2	1.1	0.1	0	0	0.2

2012-2013	0	0	0	0	0	6.5	11.8	0.7	0.1	M	0	0	1.7
2013-2014	0	0	0	0.2	0	2.6	0.5	1.2	M	0.2	0	0	0.4
2014-2015	M	0	M	0	0	M	0.1	0.1	0.1	0.3	0.8	0	0.2
2015-2016	0	0	0	0	0.5	1.5	4	1.4	0.5	0	0	0	0.7
2016-2017	0	0	0	0	0.7	1.4	M	12.1	0.5	0.1	0	0	1.3
2017-2018	0	0	0	0	0	0	0.3	0.3	1.6	0	0.1	0	0.2
2018-2019	0	0	0	0	0.3	3	4.8	19.2	2.4	0	0	0	2.5
2019-2020	0	0	0	0	0.9	5.4	2.7	0	1.1	0.5	0	0	0.9
2020-2021	0	0	0	0	0.9	2.1	6.6	24	4.3	0	0	0	3.2
2021-2022*	0	0	0	0.1	0	M	M	2.3	M	0	M	0	0.3
2022-2023*	0	0	0	0	4.9	4.4	33.8	M	52.6	22.5	0	0	10.7
2023-2024*	0	0	0	0	0	0	1	14.4	3.8	0	0	0	1.6
Mean	0	0	0	0.1	0.5	1.9	6.9	6.2	4.1	1.1	0	0	1.2
Max	0	0	0	0.9	4.9	6.5	33.8	24	52.6	22.5	0.8	0	10.7
Min	0	0	0	0	0	0	0.1	0	0	0	0	0	0
	###	2023	2023	1996	2022	2012	2023	2021	2023	2023	2015	2024	

Anomaly:

2021-2022	0	0	0	0	-0.5	M	M	-3.9	M	-1.1	M	0	-0.9
2022-2023	0	0	0	-0.1	4.4	2.5	26.9	M	48.5	21.4	0	0	9.5
2023-2024	0	0	0	-0.1	-0.5	-1.9	-5.9	8.2	-0.3	-1.1	0	0	0.4

Stream Flow Data:

Stream Flow data can be used as a proxy for precipitation volume and snow melt rates. Hydrographs with steep peaks indicate fast runoff from hillslopes to channels during rainstorm events or enhanced snow melt. The closest stream to the Mono basin and Tahoe moraines is Walker Creek; however, the USGS does not have an active stream gauge at that site. Therefore, the closest USGS stream gauge data for two flowing bodies of water in similar environments to the Tahoe and Mono basin moraine will be provided: Robinson Creek, 18 miles to the north of the field sites; and Deadman Creek, 15 miles south of the field sites.



- using custom time span
January 1, 2020 - December 31, 2024
Gage height, feet

6.71 ft - Oct 08, 2024 07:30:00 AM PDT



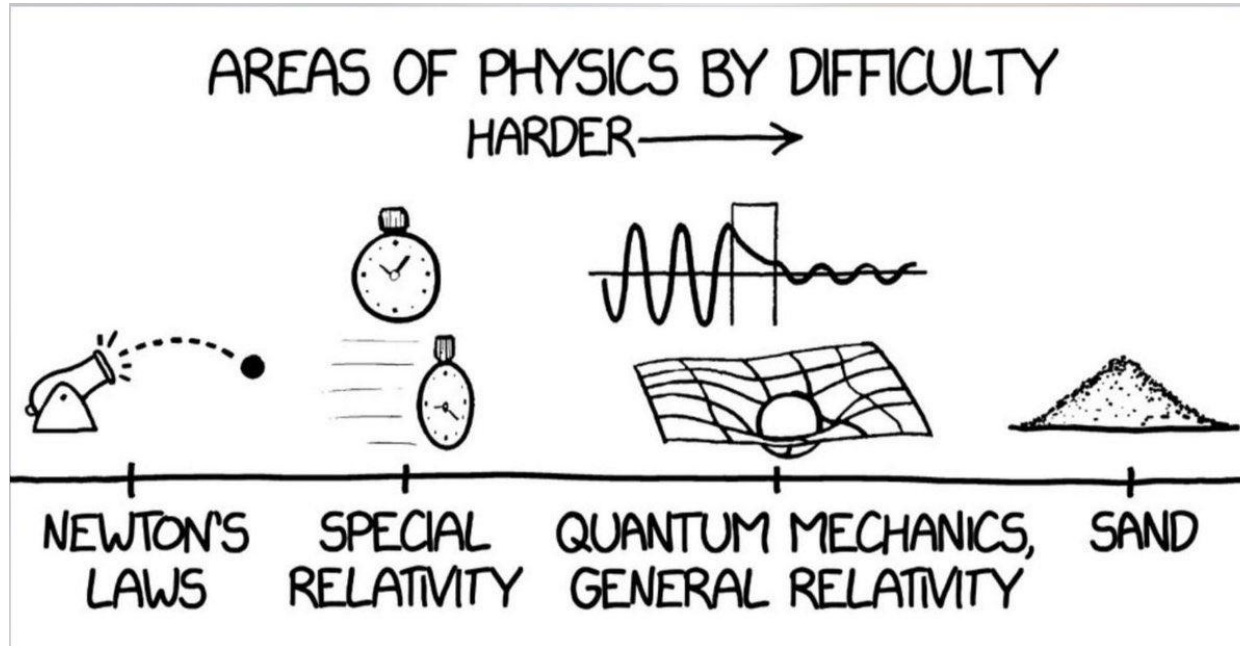


Figure 15. In physics, there are complete theories to explain gravitation in low mass and speed environments (Newton's Laws), the stretching of time when an observer approaches the speed of light (Special Relativity), the behavior of matter at resolutions reduced to the scale below that of the atom or its nucleus (Quantum Relativity), and how time, space, and matter are warped around universally massive objects (General Relativity). However, there is yet no theory of granular media, and the best simulations of their kinetic behavior are often at the grain scale, a scale often too small for reasonable computation.